# Mountain Waves, Downslope Winds, and Low-Level Blocking Forced by a Midlatitude Cyclone Encountering an Isolated Ridge

MAXIMO Q. MENCHACA AND DALE R. DURRAN

*University of Washington, Seattle, Washington*

(Manuscript received 22 March 2016, in final form 3 October 2016)

ABSTRACT

The interaction of a midlatitude cyclone with an isolated north–south mountain barrier is examined using numerical simulation. A prototypical cyclone develops from an isolated disturbance in a baroclinically unstable shear flow upstream of the ridge, producing a cold front that interacts strongly with the topography. The structure and evolution of the lee waves launched by the topography are analyzed, including their temporal and their north–south variation along the ridge. Typical mountain wave patterns are generated by a 500-m-high mountain, but these waves often exhibit significant differences from the waves produced in 2D or 3D simulations with steady large-scale-flow structures corresponding to the instantaneous conditions over the mountain in the evolving flow. When the mountain height is 2 km, substantial wave breaking occurs, both at low levels in the lee and in the lower stratosphere. Despite the north–south uniformity of the terrain profile, large north–south variations are apparent in wave structure and downslope winds. In particular, for a 24-h period beginning after the cold front passes the upstream side of the ridge toward the south, strong downslope winds occur only in the northern half of the lee of the ridge. Just prior to this period, the movement of the cold front across the northern lee slopes is complex and accompanied by a burst of strong downslope winds and intense vertical velocities.

## 1. Introduction

A variety of disturbances, including gravity (mountain) waves, downslope winds, and low-level blocking, may be produced when a stably stratified airstream encounters a topographic barrier. Mountain waves exert a decelerating force on the large-scale flow that is parameterized in large-scale weather and climate models (Kim et al. 2003), although the precise impact of this forcing is not yet well understood. As mountain waves steepen and break, they generate clear-air turbulence, posing a hazard to aviation (Bacmeister et al. 1994). Maximum gusts in downslope winds have been observed to exceed 56 m s$^{-1}$ (Brinkmann 1971), posing a threat to communities in the immediate lee of steep mountain barriers. Low-level blocking on the upstream side of a mountain may exert a major influence on orographic precipitation and pollutant transport (Hughes et al. 2009).

Most of the theoretical work on these terrain-induced disturbances has been limited to the study of mountains in steady horizontally homogeneous flows. For example, idealized numerical studies of low-level blocking by long ridges have demonstrated the dynamical importance of Coriolis forces and surface friction in steady large-scale flows with uniform winds and static stability (Ólafsson and Bougeault 1997; Zängl 2004; Wells et al. 2005). Moving toward more realistic idealizations of time-varying large-scale flows, Lott and Teitelbaum (1993a,b) examined mountain waves forced by a single cycle of acceleration and deceleration in a horizontally uniform large-scale flow and found that if the time scale for advective transport across an isolated ridge was short compared to the time scale of the variations in the large-scale flow, the near-surface mountain wave momentum flux at a given time $t_*$ was similar to that for a steady flow in which the large-scale forcing matched that instantaneously present at time $t_*$. The time required for groups of internal gravity waves to propagate upward can, however, lead to different behavior aloft. Chen et al. (2005) studied the slow passage of a dynamically consistent isolated jet over a mountain barrier and found major differences in the behavior of the vertical momentum fluxes aloft produced by a series of steady-state solutions for large-scale flows matching that of the instantaneous properties of the evolving flow. Hills and

---

*Corresponding author e-mail*: Maximo Q. Menchaca, menchaca@atmos.washington.edu

DOI: 10.1175/JAS-D-16-0092.1

Durran (2012) considered the same isolated jet with a layered static-stability structure supporting trapped waves and found the horizontal variations in the large-scale flow could untrap the lee waves as they propagated downstream. Chen et al. (2007) also identified regions where wave breaking ultimately led to a quasigeostrophically balanced region of flow deceleration well downstream of the mountain.

The isolated jet considered in these previous studies had no vertical wind shear (only horizontal variations), and the static stability was constant throughout each vertically stacked layer. In this study, we increase the realism of the idealized large-scale flow by examining the interaction of a midlatitude cyclone with an isolated long ridge. The cyclone develops upstream of the mountain in a baroclinically unstable shear flow, seeded by a localized potential vorticity (PV) anomaly. The low-level cross-mountain winds increase gradually as the cyclone and its associated cold front approach the topography, and they remain strong for a couple days after the cyclone passes to the north of the ridge.

One major motivation for considering this problem is to obtain a detailed understanding of the influence of the mountain on a prototypical large-scale weather system, and that will be the focus of a subsequent paper. Here we investigate the behavior of the waves themselves, along with the evolution of the blocked flow upstream of the mountains, the downslope winds, and the penetration of the cold front into the immediate lee of the topography. Section 2 describes the basic state, the complex procedure to initialize the large-scale cyclone, and the topography. The configuration of the numerical model is discussed in section 3. In section 4, we examine the behavior of quasi-linear waves generated by a 500-m-high mountain[1] and compare their structure at key times with that from corresponding two- and three-dimensional simulations with steady large-scale flows. Section 5 examines the much more nonlinear response, including low-level blocking and flow diversion, generated by a 2-km-high mountain. Our conclusions are presented in section 6.

## 2. The mountain and the evolving large-scale flow

Our simulations are conducted using the Advanced Research version of the Weather Research and Forecasting (WRF) Model (ARW), version 3.3.1 (Skamarock et al. 2008), to integrate the dry nonhydrostatic, compressible equations of motion. The horizontal extent of the physical domain is 16 200 km in the $x$ direction and 9000 km in the $y$ direction. We define the origin for our coordinate system to be coincident with the centerline of the mountain along the $x$ coordinate and in the north–south center of the channel along the $y$ coordinate. The feature of interest in the evolving large-scale flow is a midlatitude cyclone growing in baroclinically unstable shear. The geostrophically balanced parallel shear flow is obtained by solving (A1) in Rotunno et al. (1994) for a PV distribution with $\mathrm{PV}_s$ = 4 PV units (1 PVU = $10^{-6}\,\mathrm{K\,kg^{-1}\,m^2\,s^{-1}}$) in the stratospheric, $\mathrm{PV}_t$ = 0.4 PVU in the troposphere, and a transition-layer depth over which the PV changes of $\Delta z_{\mathrm{tr}} = 150\,\mathrm{m}$. We do, however, adopt a simpler functional form for the height of the tropopause:

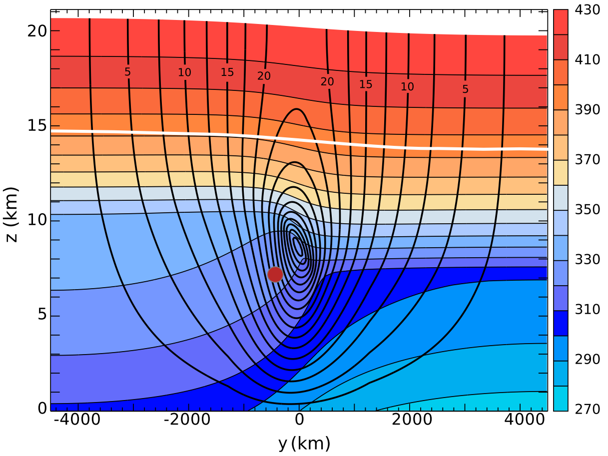

FIG. 1. North–south cross section of background shear flow: $\theta$ (colors at 10-K intervals) and zonal velocity $u$ (contoured in black at 2.5 m s$^{-1}$ intervals). The bottom of the wave-absorbing layer is indicated by the white line; the red dot shows the $y$–$z$ location of the PV anomaly.

$$z_{\mathrm{tp}} = \begin{cases} z_m - \Delta z_e \sin(\phi) & \text{if } |\phi| \le \dfrac{\pi}{2}, \\ z_m + \Delta z_e & \text{if } \phi < -\dfrac{\pi}{2}, \\ z_m - \Delta z_e & \text{otherwise}, \end{cases}$$

where $\phi = 2.65y/\Delta y_e$, $\Delta y_e$ = 600 km, and $z_m$ = 8.5 km. This formulation for $z_{\mathrm{tp}}$ allows us to obtain quiescent conditions near the north and south boundaries of the channel without introducing unrealistic tropopause slopes on each side jet axis. The Coriolis parameter is $f = 10^{-4}\,\mathrm{s}^{-1}$. After picking an initial domain height of 20.5 km, a north–south cross section through the resulting flow after performing this inversion is shown in Fig. 1.[2]

---

[1] Modest differences, characteristic of weakly nonlinear mountain waves, are evident between the wave structure in the 500-m-high-ridge simulation and those produced by a 100-m-high ridge in an additional simulation.

[2] To appreciate the difference in $z_{\mathrm{tr}}$ introduced by (2), compare Fig. 1 herein with Fig. 1 of Waite and Snyder (2009).

An isolated cyclone is triggered upstream of the topography from a finite-amplitude localized PV perturbation defined by

$$Q'(x,y,z) = Q_0 e^{-(s/\delta_h)^2} e^{-[(z-z_c)/\delta_v]^2},$$

where $Q_0$ controls the magnitude of the anomaly, $\delta_h$ and $\delta_v$ control the decay scale in the horizontal and vertical, respectively, and $s^2 = (x-x_c)^2 + (y-y_c)^2$. Parameters chosen for this study are $(Q_0, \delta_h, \delta_v, x_c, y_c, z_c) = (0.1\,\text{PVU}, 1000\,\text{km}, 300\,\text{m}, -5250\,\text{km}, -480\,\text{km}, 7\,\text{km})$, placing the anomaly slightly below and to the south of the jet core (as indicated by the red dot in Fig. 1). The horizontal and vertical scales of the PV anomaly are similar to those in Hakim (2000) and Schemm et al. (2013), but its amplitude $Q_0$ is roughly one-fifteenth as great as that used in those studies, which reduces the strength of the gravity waves generated by the initial imbalances in the nonhydrostatic governing equations.

This PV anomaly is introduced into WRF by inverting $Q'$ quasigeostrophically to determine the geopotential height and then recovering $\rho$, $u$, $v$, and $\theta$ from assumptions of hydrostatic, geostrophic, and thermal wind balance. These perturbations are then added to the zonally ($x$ coordinate) homogeneous background shear flow illustrated in Fig. 1. The resulting initial state is not in balance in the full compressible model, and the gravity waves produced by this initial imbalance would greatly complicate the analysis of the focus of our study: orographically generated mountain waves. To address this, WRF's Dolph–Chebyshev filter (Lynch 1997) was applied during a 24-h run starting from the initial condition (background shear flow plus $Q'$ induced perturbations) with a cutoff period $\tau_s = 6\,\text{h}$. A period of 24 h allows sufficient time for gravity waves generated by the initial imbalance to develop, while the choice for $\tau_s$ ensures that all such disturbances with periods less than 6 h are filtered out. The filtered variables provide a new initial condition at $t = 0.5$ days, from which the standard (unfiltered) WRF Model is integrated forward.

An isolated mountain ridge is centered at $(x_0, y_0) = (0, -480)$ km. The topographic elevation $h$ is given by

$$h(x,y) = \begin{cases} \dfrac{h_0}{16}[1+\cos(\pi r)]^4, & \text{if } r \le 1, \\ 0, & \text{otherwise}, \end{cases} \tag{1}$$

where

$$r^2 = \begin{cases} \left[\dfrac{(x-x_0)}{4a}\right]^2 + \left[\dfrac{|y-y_0| - (\beta-1)a}{4a}\right]^2, & \text{if } |y-y_0| > (\beta-1)a, \\ \left[\dfrac{(x-x_0)}{4a}\right]^2, & \text{otherwise}, \end{cases}$$

with $a = 20\,\text{km}$ and $\beta = 15$. This yields ridge approximate $x$ and $y$ extents for the ridge of 80 and 640 km, respectively. Ridge heights of both $h_0 = 500\,\text{m}$ and 2 km are considered.

The evolution of the cyclone triggered by this PV anomaly is illustrated by the surface isobars and $\theta$ fields in Fig. 2. The overall pattern is similar to that of a prototypical midlatitude cyclone, with distinct warm and cold fronts appearing by 3.5 days and an occluded front forming by 5.5 days. A new cyclone develops downstream by 6.5 days. Our main focus is on the interaction of the cyclone with the topography. At 2.5 days, the surface flow in the vicinity of the mountain is quite weak and is largely parallel to the ridge axis. By 4.5 days, the low-level flow has a substantial cross-ridge component, and the cold front is just upstream of the mountain. As the cyclone passes north of the mountain, substantial low-level winds continue to be directed across the ridge at 5.5 and 6.5 days, before gradually weakening at 7.5 days.

## 3. The numerical model

The domain is discretized with a horizontal resolution of $\Delta x = \Delta y = 15\,\text{km}$; the time step is $\Delta t = 50\,\text{s}$. The lateral boundaries are periodic in $x$ and symmetric in $y$. A fine grid, on which $\Delta x = \Delta y = 5\,\text{km}$, is nested in the subdomain $-380 \le x \le 1165\,\text{km}$, $-1125 \le y \le 750\,\text{km}$. While this resolution would be insufficient for resolving trapped lee waves, it is adequate to capture the vertically propagating waves forced by our relatively wide mountain.

The only physical parameterizations we employ are 2D Smagorinsky mixing in the horizontal and a modified version of the Yonsei University (YSU) boundary layer scheme (Hong et al. 2006) to limit the winds around the cyclone to realistic values though surface friction and vertical mixing.[3]

---

[3] Default values of the parameters are used for the boundary layer scheme, except that the heat flux is set to zero, $z_0$ is a uniform 0.01 m, and the boundary layer height is fixed at the first model level, approximately 12 m above the surface.

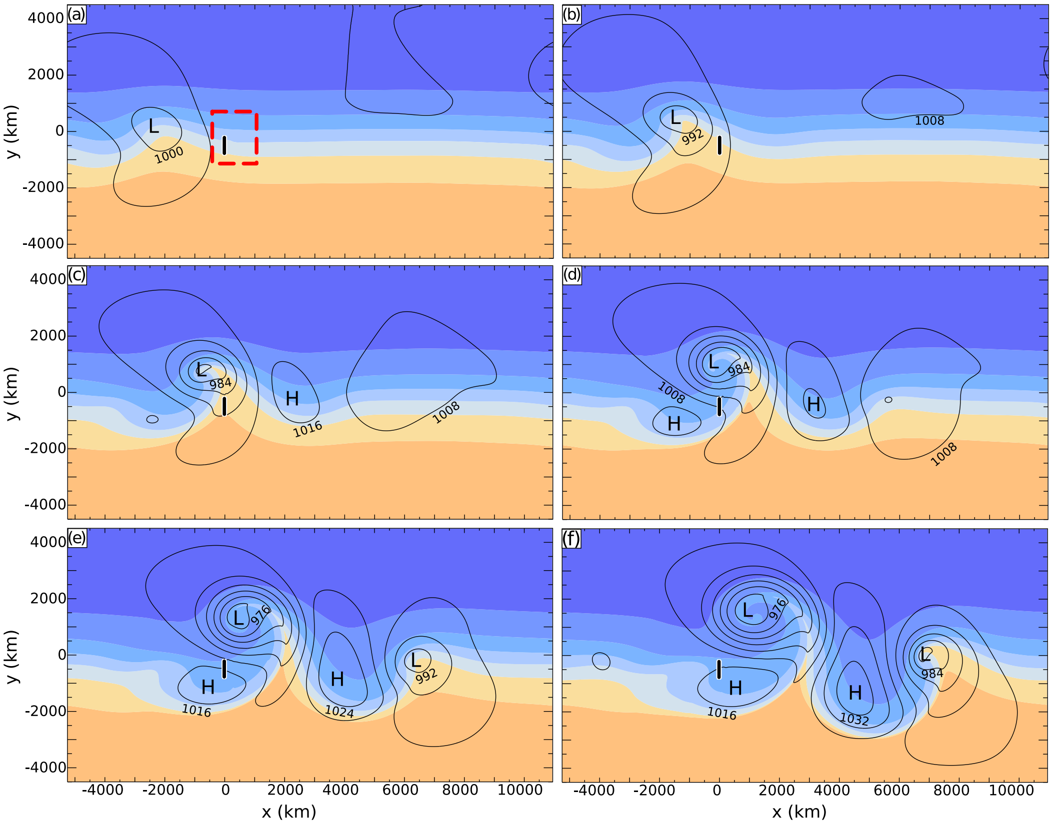

FIG. 2. Surface isobars (black lines at 8-hPa intervals) and surface $\theta$ (color fill at 5-K intervals) for the developing cyclone at (a) 2.5, (b) 3.5, (c) 4.5, (d) 5.5, (e) 6.5, and (f) 7.5 days. The mountain is depicted by the black vertical bar at $x = 0$ km in all panels. The nested grid is shown in by the red dashed square in (a). Lows and highs are labeled by an "L" and "H," respectively.

The vertical domain extends to either 20.5 or 26.5 km.[4] In the shallower domain, there are 80 vertical levels spaced at 30 m near the surface, with $\Delta z$ increasing to 400 m near the model top. A 6-km-deep Rayleigh damping layer is used to minimize gravity wave reflections off the top boundary. The damping-layer formulation follows Klemp et al. (2008), except that their damping profile [their (21)] is replaced with

$$\beta_w(\hat{z}) = \begin{cases} \dfrac{\beta_{\max}}{2}[1-\cos(\pi\hat{z})] & \hat{z} \le \dfrac{1}{2}, \\[2ex] \dfrac{\beta_{\max}}{2}\left[1+\pi\left(\hat{z}-\dfrac{1}{2}\right)\right] & \hat{z} > \dfrac{1}{2}, \end{cases} \tag{2}$$

where $\beta_{\max} = 0.4$, $\hat{z} = (z - z_b)/(z_t - z_b)$, and $z_t$ and $z_b$ are the heights of the top and bottom of the damping layer. For the same value of $\beta_{\max}$, this layer provides about 7.5% more layer-integrated damping than the expression in Klemp et al. (2008) without increasing the maximum value of $\partial\beta_w/\partial\hat{z}$ in the damping layer.

If these were strictly linear mountain waves, the upper boundary condition and domain depth could simply be specified to prevent spurious reflections of upward-propagating gravity waves into downward-propagating modes. Our waves are not linear, and as discussed in Durran and Klemp (1983), one should expect sensitivity to the location of the model top and the damping-layer configuration unless the primary regions of wave breaking and dissipation is contained within the physical domain (i.e., below the bottom of the damping layer).

To test the sensitivity of our solutions to the upper boundary configuration, a pair of simulations with 12-km-deep damping layers were also conducted using 26.5-km-deep domains. These thick-damping-layer simulations use 95 vertical levels, configured so that the first 80 levels are at identical heights and pressures to those in the 20.5-km deep domain. In these cases, the basic state depicted in Fig. 1 is extended upward to 26.5 km using constant values of the average vertical grid spacing, average Brunt–Väisälä frequency, and the

---

[4] Because of WRF's vertical coordinate, the height at model top varies slightly in space and time.

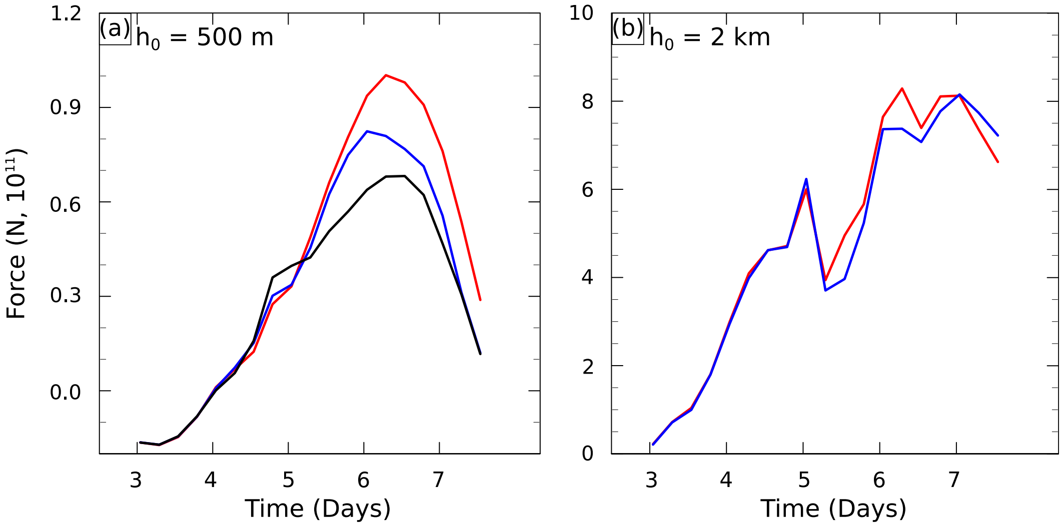

FIG. 3. The cross-mountain pressure drag for the (a) 500-m mountain and (b) 2-km mountain. Red (blue) curves are for simulations using a 6 (12)-km-deep damping layer based at 14.5 km. The black curve in (a) is from a simulation using a 6-km-deep damping layer based at 20.5 km.

average horizontal winds from the top five levels of the 20.5-km domain.

The influence of the upper boundary configuration on the evolution of the cross-mountain pressure drag,

$$P = \int\!\!\int p\frac{\partial h}{\partial x}dy\,dx,$$

integrated over the inner nest, is shown in Fig. 3. When $h_0 = 2\,\mathrm{km}$, substantial wave breaking occurs below the bottom of the damping layer, and both damping-layer configurations yield very similar results. In contrast, when $h_0 = 0.5\,\mathrm{km}$, the pressure drag produced by the standard damping layer (red curve) systematically exceeds that obtained using the thick damping layer (blue curve), beginning around 5.5 days, which is about the time that wave breaking first develops in the lower portion of each damping layer. Although they are qualitatively similar, these wave breaking regions are sufficiently different to generate nontrivial differences in the waves and the maximum values of the cross-mountain pressure drag. Therefore, we conducted another 26.5-km-deep simulation designed to shift the damping layer above this wave breaking region. The initial atmospheric state for this additional simulation matched that in the thick-damping-layer simulations, but the base of the damping layer was moved up such that $z_b = 20.5\,\mathrm{km}$, and the damping-layer structure was set to the standard 6-km-deep configuration used in the 20.5-km-deep-domain cases.

As shown by the black curve in Fig. 3a, the new simulation with $z_b = 20.5\,\mathrm{km}$ produces even weaker cross-mountain pressure drags. There is no wake breaking in this simulation, and the waves are visibly more similar to classic linear mountain waves. A representative estimate of the nonlinearity of the tropospheric mountain wave, taking 5-km-level values just upstream of the mountain of $N_l = 0.012\,\mathrm{s}^{-1}$ and $U_l = 36\,\mathrm{m\,s}^{-1}$, is $N_l h_0/U_l = 0.17$. Wave breaking was occurring around $z = 16\,\mathrm{km}$, where $N_u = 0.015\,\mathrm{s}^{-1}$ and $U_u = 28\,\mathrm{m\,s}^{-1}$. The influence of changes in density, wind speed, and static stability on the waves suggests that roughly two density scale heights above the surface, $(\rho_u/\rho_0)^{-1/2}N_u h_0/U_u = 0.74$. The threshold for wave breaking in a Boussinesq flow with constant $N$ and $U$ over a Witch of Agnesi mountain profile is $Nh_0/U = 0.85$ (Lilly and Klemp 1979), slightly larger than our estimate. Thus, it is not particularly surprising that there is no wave breaking in this last simulation.

These are very computationally intensive simulations, and it is not practical to attempt further sensitivity tests in even deeper domains that might extend to high-enough levels for the decrease in density with height to finally produce wave breaking in the $h_0 = 500$-m case. In the remainder of this paper, we therefore focus on simulations with the 6-km-deep damping layer beginning at $z_b = 20.5\,\mathrm{km}$ for the $h_0 = 500$-m ridge and at $z_b = 14.5\,\mathrm{km}$ for the $h_0 = 2$-km ridge. Further details about the pressure drags, momentum fluxes, and mountain wave–mean flow interactions will be the subject of a companion paper.

## 4. Waves generated by the 500-m-high mountain

### a. Morphology in the evolving large-scale flow

We first focus on the 500-m-high-mountain case, because, as just discussed, it both generates relatively low-amplitude perturbations similar to classical lee waves

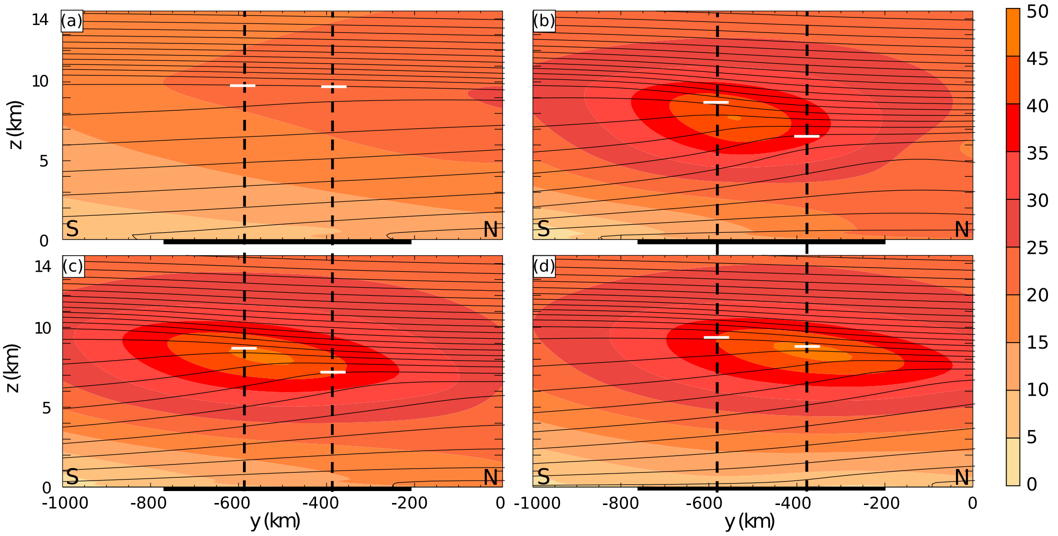

FIG. 4. Cross-mountain flow (zonal velocity $u$; colors at 5 m s$^{-1}$ intervals) and $\theta$ (contours; 5-K intervals) upstream of the ridge at $x = -200$ km at (a) 4.5, (b) 5.5, (c) 6.5, and (d) 7.5 days for the 500-m-high mountain. South is to the left in each panel. The black bar indicates the meridional extent of the mountain. Vertical dashed lines indicate the location of the $x$–$z$ cross sections in Figs. 6–9. Short white lines superimposed on these dashed lines indicate the approximate position of the tropopause.

and produces no wave breaking, which can complicate the interpretation of our results through the secondary generation of upward- and downward-propagating gravity waves (Bacmeister and Schoberl 1989; Smith et al. 2008). All figures in this section are taken from the 5-km nest. The evolution of the synoptic-scale environment is depicted 200 km upstream of the crest in Fig. 4 by $y$–$z$ cross sections of $\theta$ and zonal velocity $u$. The view is toward the west, with south on the left. As the developing cold front arrives at the mountain at 4.5 days, the upper-level winds are relatively weak, and there is little meridional gradient in the static stability below 5 km (Fig. 4a). The jet sweeps over the terrain and a day later is situated over the center of the mountain, with maximum speeds slightly greater than 45 m s$^{-1}$ (Fig. 4b). The low-level static stability is now considerably stronger to the south of the mountain than to the north, and the tropopause height is roughly 2.4 km lower at the position of the northern $x$–$z$ cross section than at the southern cross section. The jet sweeps southward of the mountain during the next 8 h, before beginning to shift back to the north. By 6.5 days, the jet is again near the center of the mountain, with static stability remaining stronger to the south of the ridge (Fig. 4c). The jet continues to shift north; at 7.5 days, its core is near the northern $x$–$z$ cross section (Fig. 4d), and, at low levels, the meridional shear in $u$ is much weaker than that during the previous 2 days. The north–south difference in the tropopause height at the location of the two $x$–$z$ cross sections is also much reduced by 7.5 days. The near-surface cross-mountain winds are strongest at 5.5 and 6.5 days (Figs. 4b,c).

The morphology of the evolving mountain waves is shown by a series of cross sections of the vertical velocities and isentropes at the same times depicted in Fig. 4. Figure 5 shows a $y$–$z$ cross section 20 km downstream of the crest, where the terrain elevation has dropped to 250 m. The dashed vertical lines in Figs. 4 and 5 show the location of a pair of $x$–$z$ cross sections 100 km north and south of the center of the terrain, which appear in Figs. 6–9; likewise, the dashed vertical line in Figs. 6–9 shows the location of the $y$–$z$ cross sections in Fig. 5. Note that while the contour interval is identical for Figs. 6–9, the range of the vertical velocity magnitude does change.

We first focus on the general structure of the waves in the evolving-flow simulation described above, which is depicted in Fig. 5 and Figs. 6a,b, 7a,b, 8a,b, and 9a,b. At 4.5 days, just prior to frontal passage, the relatively slow cross-mountain flow (Fig. 4a) produces weak mountain waves that are roughly uniform from north to south along the ridge, with maxima present in the upper troposphere (Figs. 5a and 6a,b). One day later, the cross-mountain flow is stronger, the tropopause has dropped noticeably (by about 3 km in the north), and there is more variation in the wave structure along the ridge (Figs. 5b and 7a,b). The waves in the northern cross section are stronger and extend farther down the lee slope than those in the south (Fig. 7a,b). Strong vertical velocities are present just downstream of the ridge at $x =$ 50 km in the northern cross section; in contrast, there is

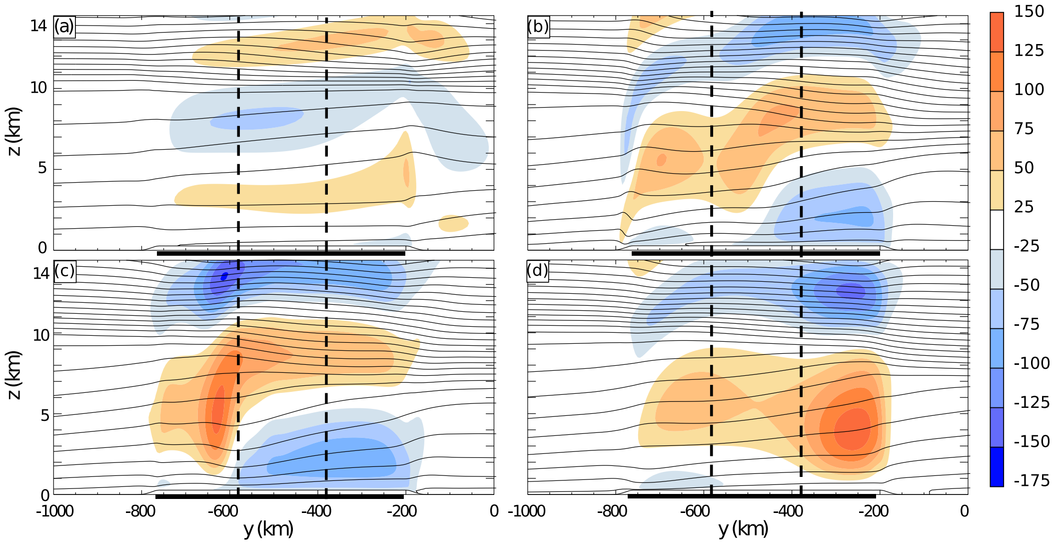

FIG. 5. Cross sections of $w$ (colors; 25 cm s$^{-1}$ intervals) and $\theta$ (contours; 5-K intervals) downstream of the ridge at $x = 20$ km at (a) 4.5, (b) 5.5, (c) 6.5, and (d) 7.5 days for the 500-m-high mountain. The vertical dashed lines indicate the location of the $x$–$z$ cross sections in Figs. 6–9.

no strong vertical velocity signature downstream of the terrain in the southern cross section.

The waves at 6.5 days are stronger still, and the most intense waves have shifted to the southern part of the mountain (Fig. 5c). In comparison with the north (Fig. 8b), the vertical velocity perturbations in the south are much narrower and more upright, with a deep region of ascent throughout the central and upper troposphere, centered at $x = 30$ km (Fig. 8a).

Finally, at 7.5 days, the slackening of the low-level cross-mountain flow leads to weaker wave activity everywhere except at the north end of the mountain (Fig. 5d). The waves in the $x$–$z$ cross sections (Fig. 9a,b) are also stronger to the north. Overall, the north–south progression of the waves between days 5.5 and 7.5 is qualitatively similar to that of the jet maximum in the upstream flow (Figs. 4b–d): strong wave activity shifts south with time, before moving back toward the north (Figs. 5b–d).

Large differences in the vertical velocities between the northern and southern legs were observed along repeated transects 50 km apart over the Sierra Nevada during the T-REX field campaign (Doyle et al. 2011). Similar overall contrasts (roughly a factor of 2) between the northern and southern transects appear in these simulations, although much larger contrasts can be obtained at specific altitudes (e.g., at 12 km in Figs. 7a and 7b or 4 km in Figs. 8a and 8b). These north–south differences are forced by the nonuniform mean flow (as we have no variations in the underlying terrain), whereas in T-REX they were attributed to differences in the underlying terrain. In our simulations, however, there is a 200-km separation between the legs, which is 4 times larger than that in T-REX. The 500-m-high mountain in the preceding simulations is also much lower than the Sierra Nevada. As will be discussed in section 5, even larger north–south differences can appear when the mountain height is increased to 2 km, but the north–south contrast at a given time is not always consistent with that obtained here for the 500-m mountain.

### b. *Comparison with steady-state solutions*

The strong temporal and spatial variations in the mountain waves described in the preceding section motivate an important question: to what extent do the 1) transient and 2) north–south variations in the large-scale flow contribute to the complex wave structure? This question is important because essentially all gravity wave–drag parameterizations estimate mountain wave momentum fluxes assuming they are produced by steady waves forced by a horizontally homogeneous large-scale flow with properties that match the instantaneous conditions over the mountain. To address this question, we have performed 2D and 3D simulations with steady large-scale forcing. Both the north–south wind shear and the time dependence of the large-scale flow have been removed from the 2D simulations, while only the time dependence has been removed from the 3D simulations. The Coriolis force is set to zero in the 2D simulations and to $f = 10^{-4}$ s$^{-1}$ in the 3D cases.

The 2D simulations are forced by a steady upstream flow in which profiles of $u$ and $\theta$ match those from the evolving-forcing simulations at a point $L_u = 200$ km

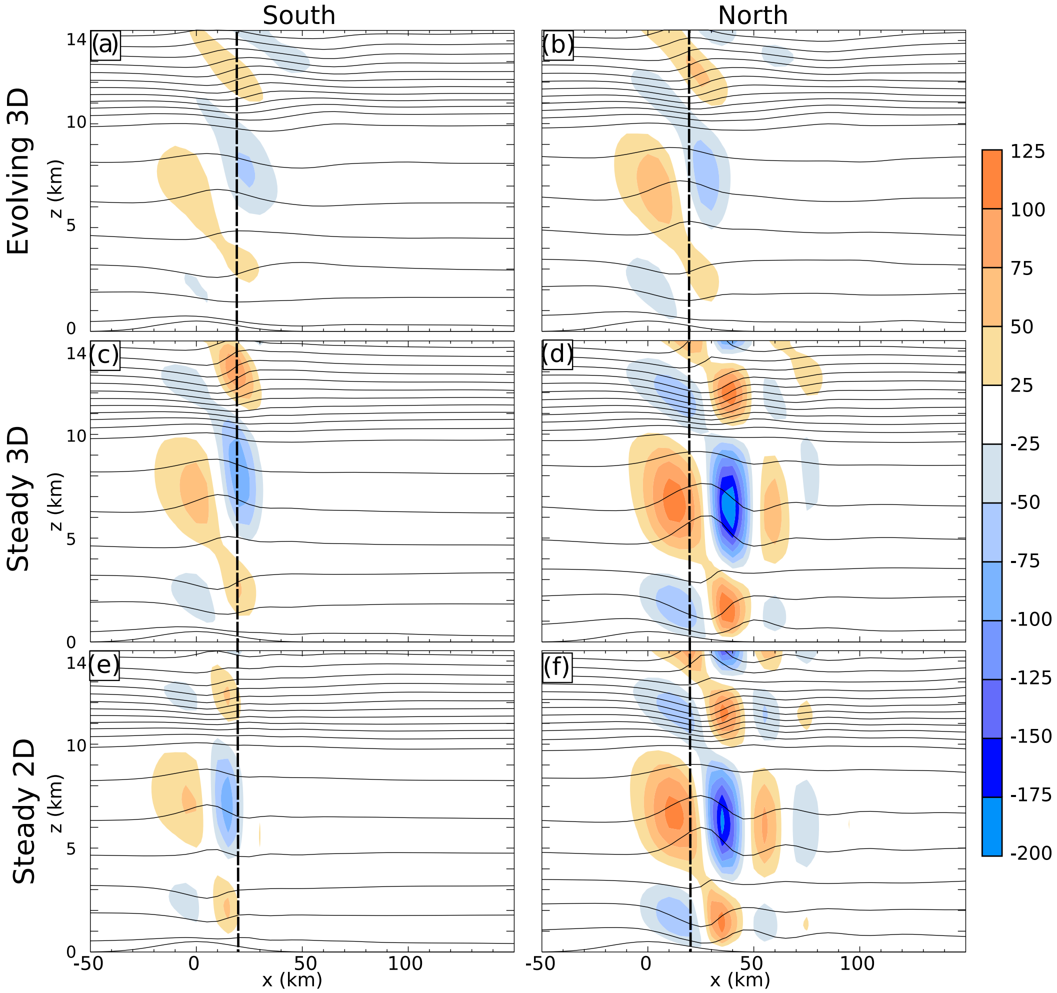

FIG. 6. Vertical cross sections of $w$ (colors; 25 cm s$^{-1}$ intervals) and $\theta$ (contours; 5-K intervals) from the 500-m-high-mountain simulations at 4.5 days. (a),(c),(e) The southern section and (b),(d),(f) the northern section. (top) The evolving-forcing simulation, (middle) the steady-forcing 3D simulations, and (bottom) the steady-forcing 2D simulations. The vertical dashed lines indicate the location of the $y$–$z$ cross section in Fig. 5.

upstream of the terrain and either 100 km north or south of the centerline. Letting $x_u$ denote the $x$ coordinate $L_u$ upstream of the crest, the parallel shear flow forcing the 3D simulations is reconstructed using the thermal wind relation from $\theta(x_u, y, z)$ and the $x$-component winds at the surface $u(x_u, y, 0)$. These reconstructed winds generally agree well with the zonal winds from the evolving-forcing simulation; the main differences occur near the jet stream core, where the winds in the steady simulations are slightly stronger. To best match the waves over the mountain at time $T_i$ (where $T_i = 4.5, \ldots, 7.5$ days), upstream conditions were extracted from the evolving-forcing simulation at the hour closest to $T_i - L_u/U_{5_i}$, where $U_{5_i}$ is the $x$-component wind over the center of the terrain at an elevation of 5 km and time $T_i$.

In the 3D steady-forcing simulations, both the size and configuration of the computational domain and the location and shape of the terrain match those on the 5-km nested grid in the evolving-forcing simulations (see Fig. 2a). The 2D simulations use the grid and topography from the corresponding $x$–$z$ slice through the nested grid. All results for the cases with steady forcing are shown after 24 h of simulation, by which time the waves reach a nearly steady state.

The vertical velocities and isentropes in the previously considered northern and southern $x$–$z$ cross sections from the steady-forcing 3D simulations are plotted in Figs. 6c,d, 7c,d, 8c,d, and 9c,d. The steady-forcing 2D simulations appear in Figs. 6e,f, 7e,f, 8e,f, and 9e,f. Recall that the corresponding results for the evolving upstream flow are plotted in Figs. 6a,b, 7a,b, 8a,b, and 9a,b.

First, consider the two times when the waves are weakest and the differences in wave structure between the northern and southern cross sections are the

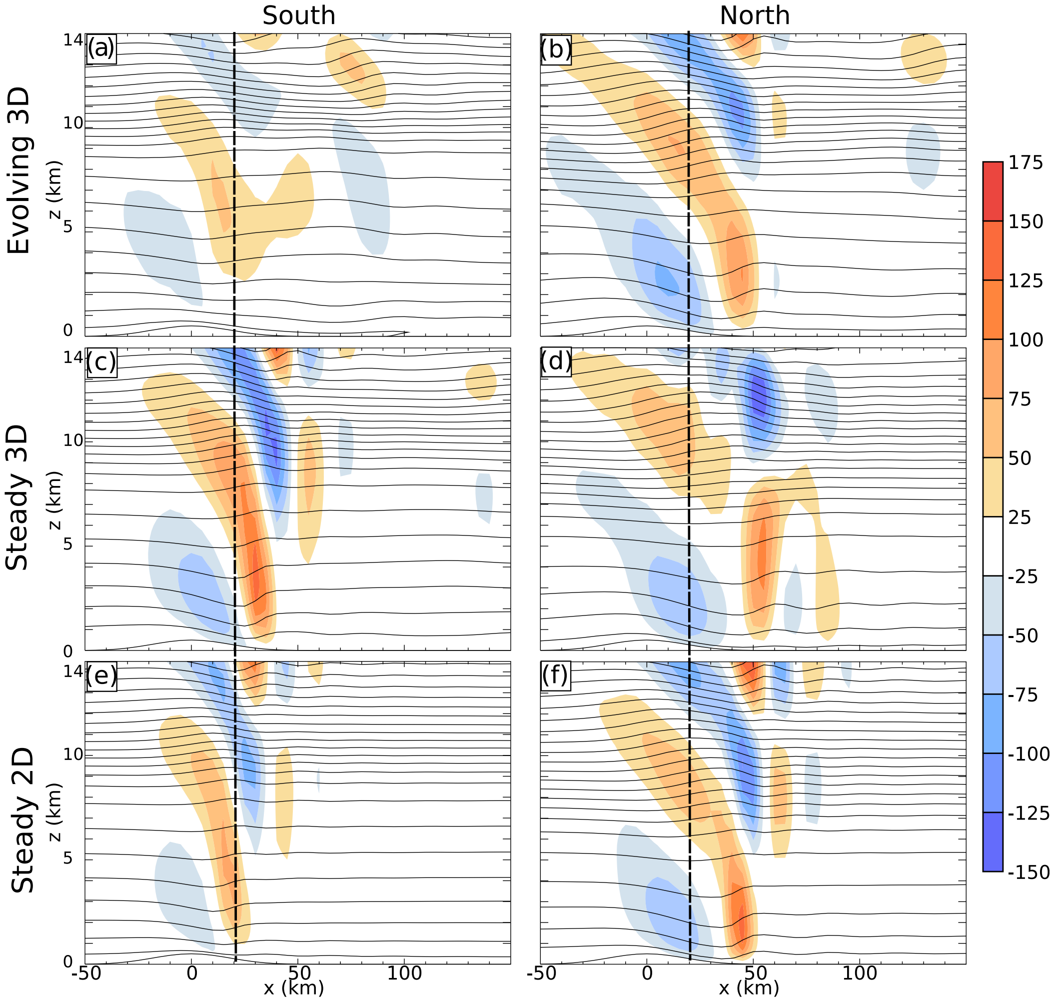

FIG. 7. As in Fig. 6, but at 5.5 days.

smallest, 4.5 and 7.5 days. While the steady-forcing simulations can reproduce the shape of the evolving-forcing simulations, the steady-forcing solutions are stronger than those for the evolving flow at 4.5 days (Fig. 6) and weaker at 7.5 days (Fig. 9), and the differences are most extreme in the northern cross sections. It is tempting to attribute these amplitude differences to a simple time lag arising because the evolving environment is less suitable for strong mountain waves prior to the conditions over the mountain at 4.5 days and more suitable for strong waves prior to the conditions at 7.5 days. However, at both times significant differences are present in the amplitude of the vertical velocities near the surface, where the waves might be expected to respond very quickly to changes in the large-scale environment.

The time required for the dominant 40-km-wavelength disturbance to propagate through the depth of the troposphere is quite short compared to the time over which the large-scale flow undergoes significant change. The vertical group velocity of a steady hydrostatic mountain wave in an flow with uniform $N$ and cross-mountain wind $U$ is $2\pi U^2/N\lambda$, where $\lambda$ is the horizontal wavelength. The waves in these simulations occur in a strongly sheared cross-mountain flow, so this formula can only provide a crude estimate. Nevertheless setting $U$ to the mean tropospheric wind speed of 17.5 m s$^{-1}$ at 4.5 days and 25 m s$^{-1}$ at 7.5 days, wave packets consisting of 40-km-wavelength waves launched at the surface would propagate to a height of 10 km in roughly 35 and 20 min at 4.5 and 7.5 days, respectively.[5] Such rapid propagation suggests the waves in the evolving-forcing simulation might be expected to have ample time to adjust to slightly different steady-state conditions, yet, as noted for a simpler case in Chen et al.

---

[5] The value of $N$ averaged over the depth of the troposphere is roughly 0.010 s$^{-1}$ at 4.5 days and 0.012 s$^{-1}$ at 7.5 days.

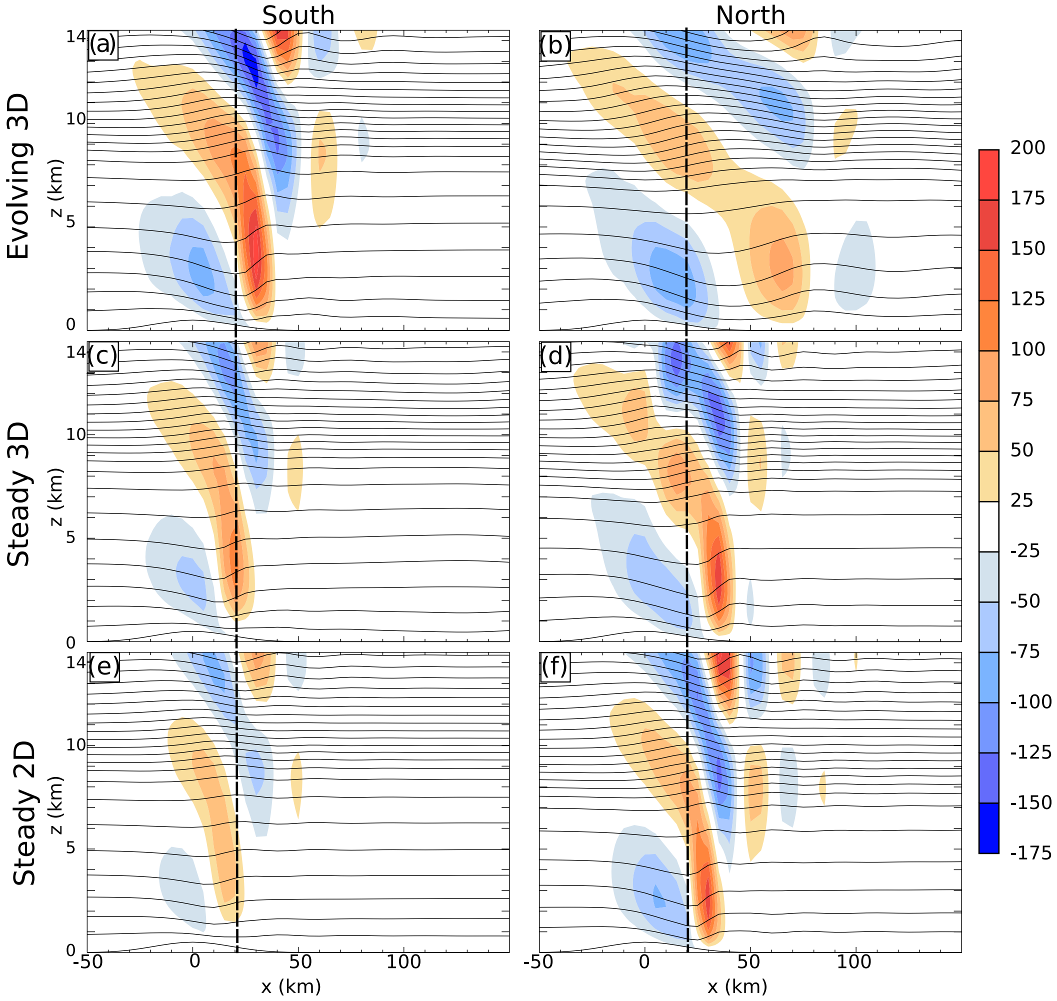

FIG. 8. As in Fig. 6, but at 6.5 days.

(2005), the waves in the slowly evolving flow do differ from those generated by truly steady forcing. The difference can be particularly pronounced when considering products of the wave perturbation fields, such as momentum flux. The wave drag, momentum fluxes, and wave–mean flow interactions in these simulations will be analyzed in a subsequent paper.

The waves are stronger at 5.5 and 6.5 days, and the differences between the waves in the steady- and evolving-forcing simulations are more complex. At 5.5 days, the waves in evolving large-scale flow (Fig. 7a) are weaker than those in the steady-forcing simulations along the southern cross section (Figs. 7c,e). Yet along the northern cross section, the waves in Fig. 7b are stronger above the mountain, but weaker in the lee, compared to those in Figs. 7d and 7f. The amplitude relationships are reversed at 6.5 days: the waves along the southern cross section in the evolving-flow simulation have become stronger than those in the steady-forcing simulations, but in the north it is the steady large-scale flow that generates stronger waves, at least in the region above the foot of the lee slope ($30 \leq x \leq 40$ km in Fig. 8).

As suggested by the preceding discussion, significant differences can develop at specific times and locations between the waves in the evolving flow and those generated by steady forcing. To better assess the aggregate magnitude of these differences on the ridge-scale response, the root-mean-square differences (RMSD) in the vertical velocity $w_\Delta$ are computed along the coordinate parallel to the ridge axis at every $(x, z)$ location for the four times at which 3D steady-forcing simulations are available: that is,

$$w_\Delta(x,z,t) = \frac{1}{N_y}\left\{\sum_{y_i}[w_e(x,y_i,z,t) - w_s(x,y_i,z,t)]^2\right\}^{1/2}, \tag{3}$$

where $w_e$ and $w_s$ are the vertical velocities in the evolving-flow steady-forcing cases, and $y_i$ are the $N_y$ gridpoint

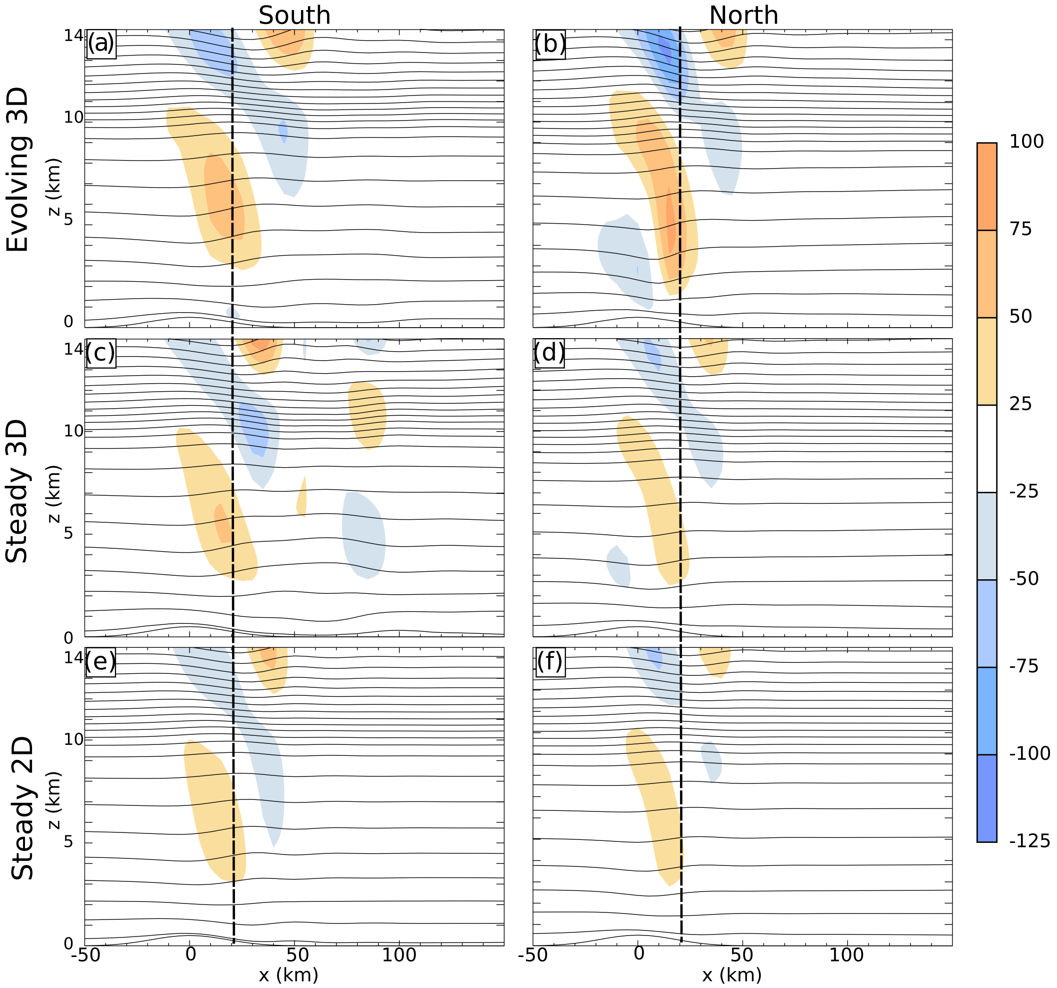

FIG. 9. As in Fig. 6, but at 7.5 days.

values satisfying $|y - y_0| \leq (\beta - 1)a$. Contour plots of $w_\Delta(x, z, t)$ are shown at $t = 4.5, \ldots, 7.5$ days in Fig. 10. At 4.5 days, $w_\Delta$ generally exceed the magnitudes of $w$ plotted in Figs. 6a and 6b. By 5.5 days, the region of $w_\Delta$ exceeding $0.25\,\mathrm{m\,s^{-1}}$ has expanded to include most of a 70-km-wide region downstream of the mountain crest (Fig. 10b); this broad distribution is due to the varied positions of waves well downstream of the crest in both the evolving-flow and steady-forcing simulations (Figs. 7a–d). The vertical velocity extrema in the evolving flow at 6.5 days grow to roughly $2\,\mathrm{m\,s^{-1}}$ (Figs. 8a,b), when the maximum $w_\Delta$ approaches $1.3\,\mathrm{m\,s^{-1}}$. Finally, at $t = 7.5$ days, the extrema in $w_\Delta$ (Fig. 10d) are comparable to the extrema of $|w|$ in the south and roughly half as large as the extrema in the north (Figs. 9a,b). Thus, at all four times, there is a substantial quantitative difference between the waves in the evolving-flow and steady-forcing simulations.

## 5. Disturbances generated by the 2-km-high mountain

We now consider the interactions of the same evolving flow with a 2-km ridge. Nonlinear processes, such as wave breaking and flow blocking, are clearly evident in this case. As before, there exist north–south differences in the mean state that change the local characteristics of the mountain waves. In addition, there are differences in the degree of nonlinearity in the wave response related to north–south variations in the nondimensional mountain height, $\tilde{N}h_0/\tilde{U}$, where $\tilde{N}$ and $\tilde{U}$ are values of the Brunt–Väisälä frequency and cross-mountain wind speed 100 km upstream of the crest averaged vertically from the surface to twice the height of the mountain. This vertical averaging strategy follows that in Ólafsson and Bougeault (1997) to facilitate comparison with earlier work. Nevertheless, as noted by Reinecke and

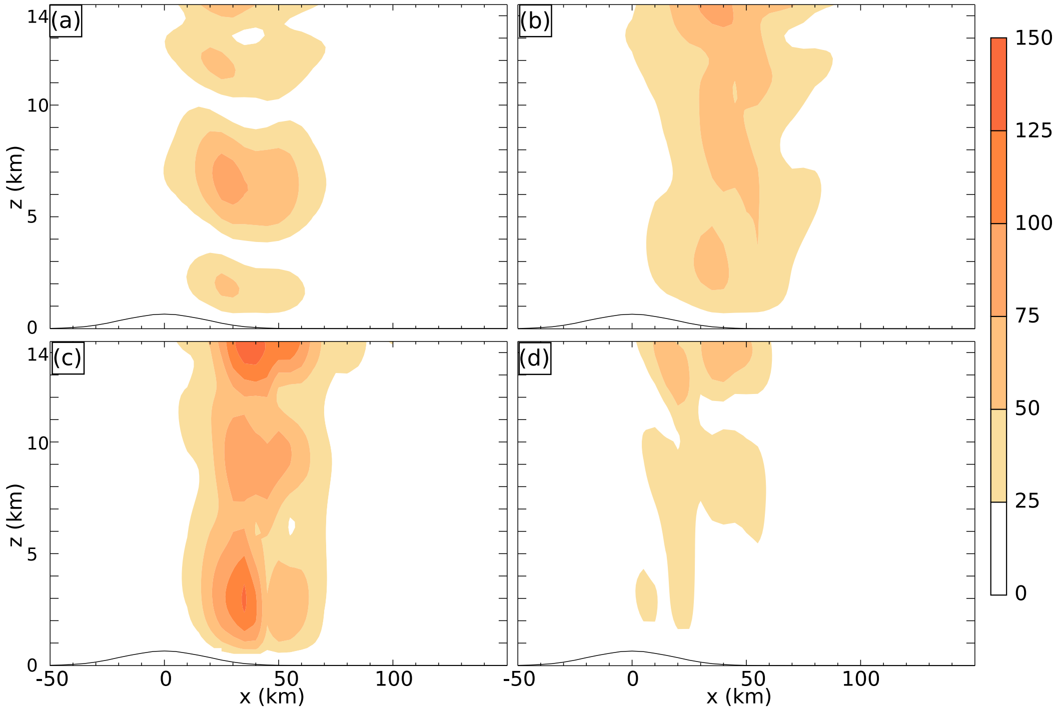

FIG. 10. North–south-averaged RMSD $w_\Delta$ in the vertical velocity (25 cm s$^{-1}$ intervals) between the evolving-flow and steady-forcing simulations for flow over the 500-m-high mountain at (a) 4.5, (b) 5.5, (c) 6.5, and (d) 7.5 days.

Durran (2008), there is no uniquely superior averaging strategy that maps vertically varying values of $N$ and $U$ to the theoretically well-studied constant-$N$ and constant-$U$ parameter space.

### a. Wave morphology

The north–south distribution of the $w$ and $\theta$ fields 20 km east of the crest of the 2-km-high mountain is shown in Fig. 11, which may be compared with the corresponding result for the 500-m mountain in Fig. 5. The wave activity strengthens after the cold front and the jet streak associated with the cyclone approach the ridge around day 4. At 4.5 days, short-wavelength perturbations, which are produced by wave breaking, are evident in the midtroposphere in both the $u$ and $\theta$ fields. As in the 500-m-high mountain case, the larger-scale

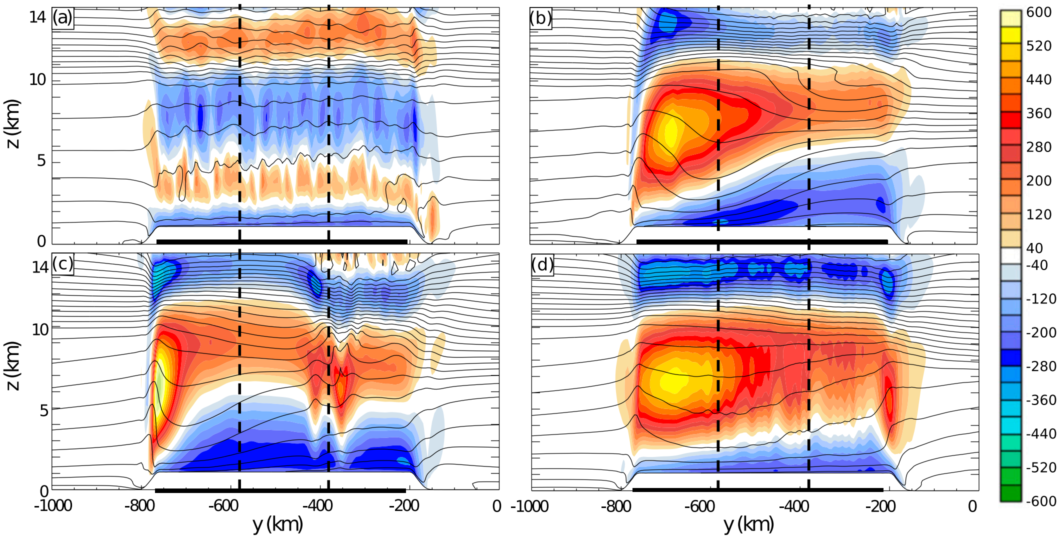

FIG. 11. As in Fig. 5, but for the 2-km mountain. The $w$ contour interval is now 40 cm s$^{-1}$. The vertical dashed lines indicate the location of the cross section in Fig. 12.

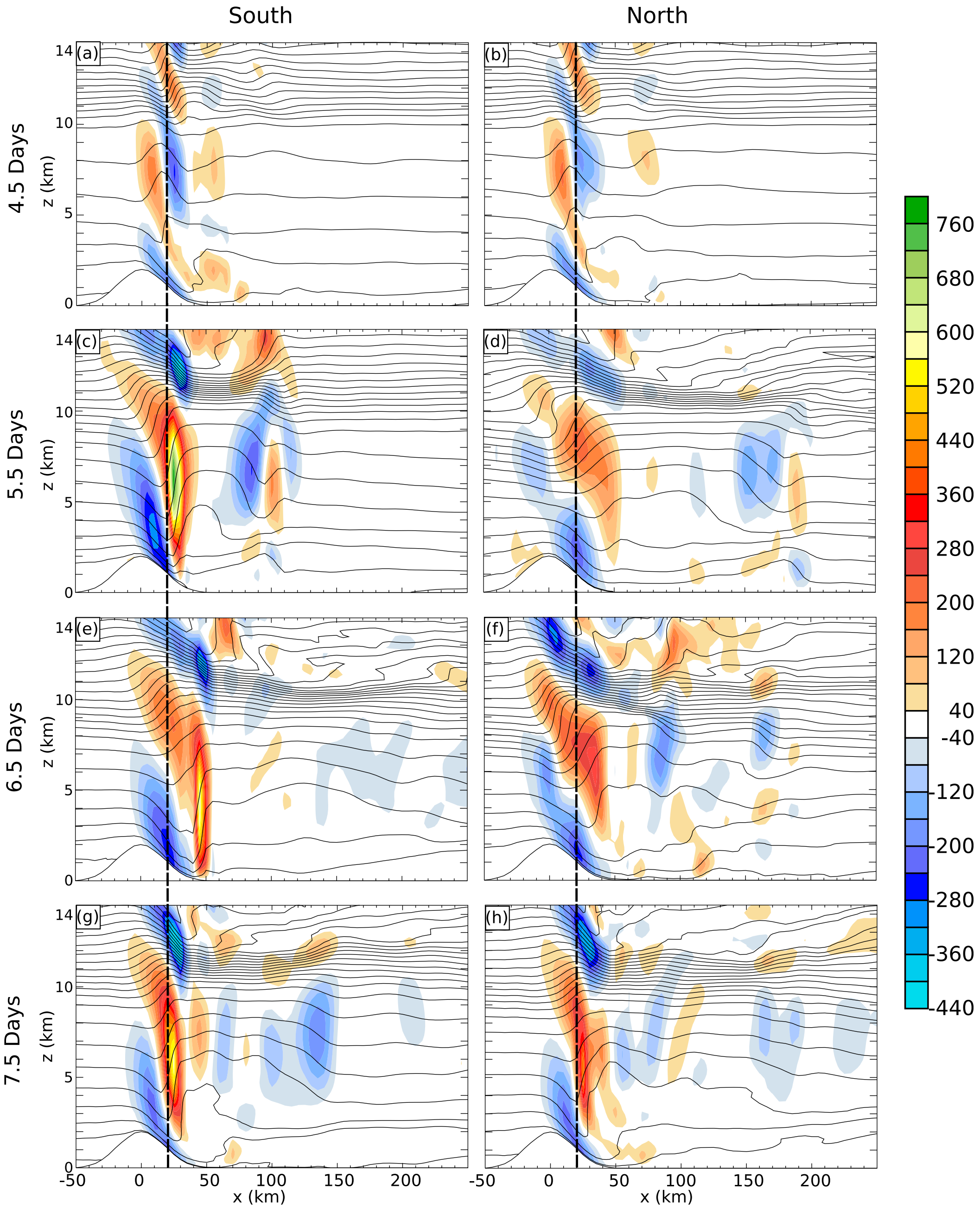

FIG. 12. Vertical cross sections of $w$ (colors; 40-cm intervals) and $\theta$ (contours; 5-K intervals) from the 2-km simulations. (left) The southern cross section and (right) the northern cross section for days (a),(b) 4.5, (c),(d) 5.5, (e),(f) 6.5, and (g),(h) 7.5, respectively. The vertical dashed lines indicate the location of the cross section in Fig. 11.

wave structure is relatively homogeneous along the entire width of the mountain, and the wave structure looks quite similar in the two east–west cross sections shown in Figs. 12a and 12b. The north–south variations in $\tilde{N}h_0/\tilde{U}$ (Table 1) at 4.5 days are also small. By 5.5 days, the increase in cross-mountain winds reduces the value of $\tilde{N}h_0/\tilde{U}$ to 1.3 upstream of the northern cross section and to 1.8 in the south, where the lower-tropospheric winds are somewhat weaker (Fig. 4b). Unlike the case for the 500-m mountain, the waves are stronger in the south, and both east–west cross sections show extensive regions of wave breaking in the stratosphere (Figs. 12c,d).

The waves are sufficiently nonsteady that systematic variations in north–south intensity cannot be adequately

TABLE 1. Nonlinearity parameter $\tilde{N}h_0/\tilde{U}$ for the $h_0 = 2$-km mountain evolving-flow simulations 100 km upstream of the crest for the cross sections depicted in Figs. 6–9 and 12. The vertical averages used to compute $\tilde{N}$ and $\tilde{U}$ extend from the surface to $z = 2h_0$.

| Time (days) | South | North |
|---|---|---|
| 4.5 | 2.3 | 2.1 |
| 5.5 | 1.8 | 1.3 |
| 6.5 | 1.9 | 1.6 |
| 7.5 | 2.5 | 2.4 |

diagnosed simply by comparing the snapshots of $w$ and $\theta$ in the east–west cross sections in Fig. 12. To better assess these temporal variations, the evolution of the maximum vertical velocity $w_{\max}$ in each cross section between days 3 and 7.5 is shown in Fig. 13; the maxima are taken over the region below $z = 10$ km beginning at the ridge crest and extending 100 km downstream. Wave breaking produces high-frequency oscillations in $w_{\max}$ for both cross sections beginning about 4 days. At about 4.5 days, the 5-h running mean of $w_{\max}$ begins to increase more rapidly in the northern cross section, where it peaks at about 5.1 days and then rapidly decreases to a relative minimum at around 5.5 days. A similar peak in the 5-h running mean of $w_{\max}$ occurs in the south at 5.5 days; the 0.4-day delay is produced by the time required for the postfrontal jet to transition between the northern and southern cross sections. This southward large-scale progression is responsible for the differences between the wave amplitudes in the northern and southern cross section evident in Figs. 12c and 12d.

After reaching a local maximum at 5.5 days, the 5-day-average $w_{\max}$ in the south drops to a local minimum similar to that experienced in the north, but it then rises rapidly, recovering to about 6 m s$^{-1}$ around 6.5 days, and remains strong through the end of the simulation. Very strong episodic wave breaking events occur in the north at 6.5 days; these are most clearly visible as the two patches of strong upward motion centered around the northern cross section (at $y = -380$ km) in Fig. 11c. At 6.5 days, the nonlinearity parameter in the south (1.9) remains somewhat larger than in the north, where $\tilde{N}h_0/\tilde{U} = 1.6$. Consistent with Fig. 13, the vertical velocities in the southern cross section are again much stronger than those in the north at 6.5 days (Figs. 12e,f).[6] By 7.5 days, the large-scale winds have decreased, the low-level static stability has increased along the entire mountain, and $\tilde{N}h_0/\tilde{U}$ is approximately 2.5 in both cross sections. As evident in Figs. 11, 12g, 12h, and 13, the waves at 7.5 days are stronger in the south, whereas they were stronger in the north in the 500-m-mountain simulation.

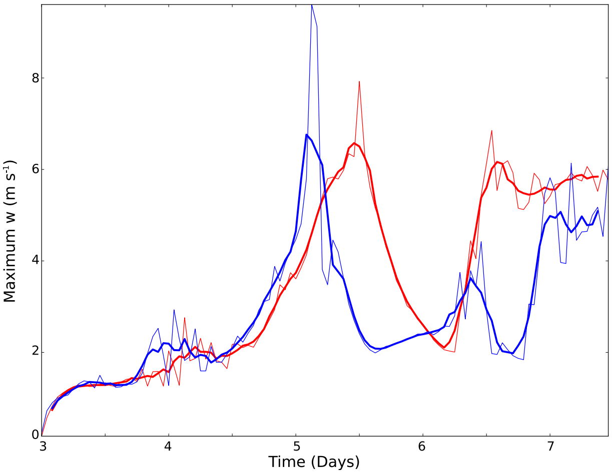

FIG. 13. Temporal variation of the maximum updraft velocities in the lee of the crest within the northern (blue) and southern (red) cross sections shown in Fig. 12. Thin lines are instantaneous values, while thick lines are averaged over 5 h.

The horizontal structure and evolution of the waves at an elevation of 8 km (about the height of the maximum winds in the jet; see Fig. 4) are shown by the vertical velocities contoured in Fig. 14. At 4.5 days, the primary updrafts and downdrafts are organized into lines above the lee slope, parallel to the ridge crest. A secondary line of updrafts, which has a modest, but a distinct southwest–northeast (SW–NE) tilt is also present about 50 km downstream of the crest. Shorter wavelength perturbations indicative of wave breaking are also present. By 5.5 days and at all later times, the primary updraft has shifted downstream and is centered above the lee slope, while a downdraft is positioned upstream of the crest. The other major feature evident at 5.5 days is the line of downward velocities extending northeastward from the southern end of the ridge; the angle between this line and the topography increases almost linearly with time between 4.5 and 5.5 days as if a hinge were swinging open about a pivot at the southern end of the topography. Similarly oriented lines of downdrafts extending from the southern end of the ridge are also apparent at 6.5 and 7.5 days, although at both these times there are also lines of downdrafts oriented from northwest to southeast in other portions of the wake.

Wave clouds have been observed angling away from the crest of the Colorado Front Range, as shown in Fig. 15, which is a view to the south from Boulder, Colorado. If these clouds were parallel to the Front Range, they (like the mountains themselves) would

---

[6] Note that the extremum in the south, visible at $x = 55$ km in Fig. 12e, is downstream of the location of the north–south cross section plotted in Fig. 11.

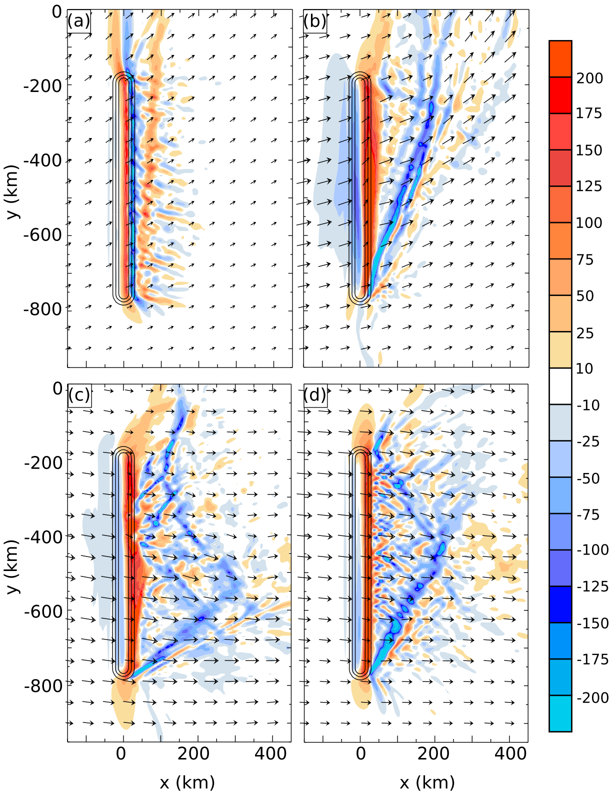

FIG. 14. Contours of *w* (colors) and horizontal wind vectors at a height of 8 km and at time (a) 4.5, (b) 5.5, (c) 6.5, and (d) 7.5 days for the evolving-forcing simulation with a 2-km-high mountain. The terrain is contoured at 0.5, 1, and 1.5 km.

FIG. 15. Quasi-steady wave cloud angling to the southeast of the Colorado Front Range on 4 Jan 1980. The point labeled "S" marks the southern point on the horizon. Photo taken by the second author in Boulder, Colorado.

appear to converge at the point "S" on the southern horizon. Clouds with this north-northwest–south-southeast orientation were visible most of the day on 4 January 1980.[7] These clouds would not be produced directly by vertical motions like those in Fig. 14b, but they show that mountain waves do indeed develop along lines angled away from the ridge axis.

The temporal evolution of the flow is a key factor in the generation of the line of downdrafts extending northeastward away from the southern edge of the mountain. Figure 16 shows the same information as Fig. 14, but for 3D simulations with steady upstream conditions matching those in the evolving flow at 4.5, 5.5, 6.5, and 7.5 days. The results for the steady-forcing simulations are shown at hour 20, at which time the cross-mountain pressure drag and low-level momentum fluxes are quasi steady. The lateral shear in the large-scale horizontal winds contributes to the generation of short SW–NE-oriented downdraft regions near the southern edge of the ridge in the steady-forcing 5.5- and 6.5-day simulations, but these regions are much less extensive than those in the evolving-forcing simulation. Moreover, the pronounced SW–NE-oriented downdraft

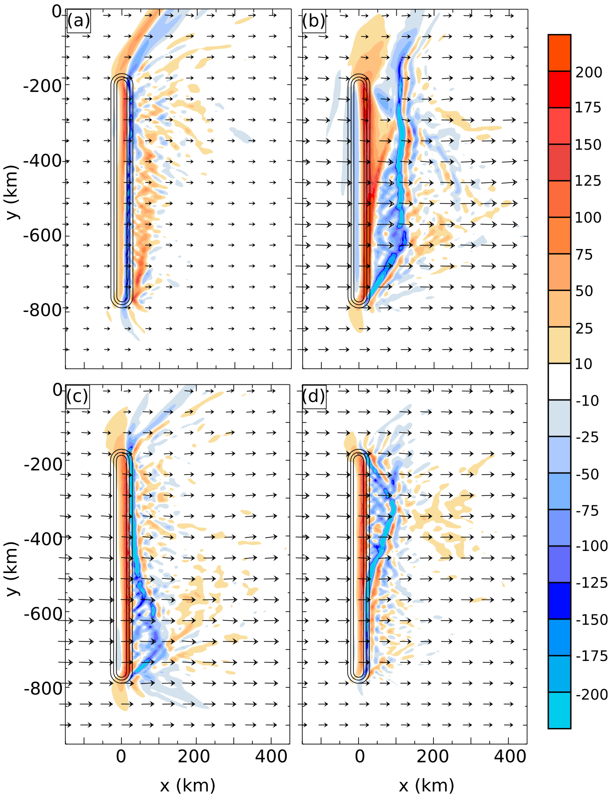

FIG. 16. As in Fig. 14, but from hour 20 of the 3D steady-forcing simulations conducted using upstream data from the evolving large-scale flow at (a) 4.5, (b) 5.5, (c) 6.5, and (d) 7.5 days.

---

[7] Field notes, photographs, and a time-lapse movie were taken by the second author. Time lapse of this feature, covering roughly 1 h of real time, appears at 4:23 in the video (https://youtu.be/P84WoxbDXCg).

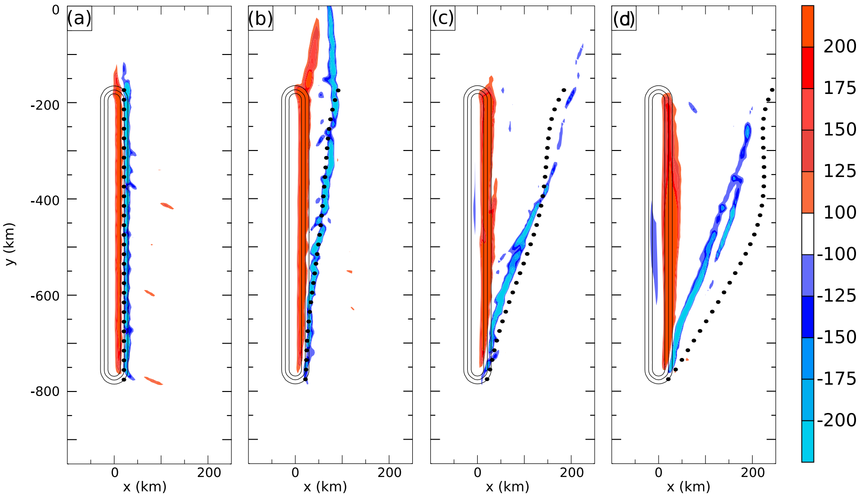

FIG. 17. The influence of lateral shear on the position of the downstream downdraft. Color contours (cm $s^{-1}$) show the 8-km vertical velocities at (a) 4.75, (b) 5, (c) 5.25, and (d) 5.5 days. The dots show the positions of passive tracers advected by the shear in the horizontal velocity, as discussed in the text.

at 7.5 days in the evolving flow (Fig. 14d) is completely absent in the corresponding steady-forcing simulation (Fig. 16d).

The angled line of downdrafts in Fig. 14 does not simply drift downstream as the cross-mountain flow intensifies. One part of the wave, the updraft, remains stationary above the lee slope, as illustrated by the vertical velocities at $z = 8$ km from the simulation with the evolving large-scale flow at 6-h intervals between 4.75 and 5.5 days shown in Fig. 17. Also shown in Fig. 17 are black dots marking the locations of passive tracers released along a north–south line from the positions shown in Fig. 17a. These tracers are followed as they are carried horizontally by the lateral wind shear vector $[u_{600}(y, t) - u_{600}(-775, t), 0]$, where $u_{600}$ is the zonal wind at 100 km upstream of the mountain at 600 hPa, and −775 km is the $y$ coordinate of the southern end of the ridge. The black dots transported by the wind shear closely follow the line of downdrafts as it shifts downstream between 4.5 and 5.25 days, but after 5.5 days the line becomes stationary while the tracers continue downstream. Further investigation of the complex dynamics responsible for this evolution of the wave structure is left for future work.

The along-ridge averaged RMSD between vertical velocities in the evolving-flow and steady-forcing simulations, $w_\Delta$ computed from (3), are shown for days 4.5–7.5 in Fig. 18; the data for the steady-forcing simulation are again taken from hour 20. As was the case for the 500-m-high mountain, the values of $w_\Delta$ approach the magnitudes of vertical velocities in the evolving flow. For example, at 7.5 days, the maximum value of $w_\Delta$ exceeds 5.6 m $s^{-1}$, while the largest $w$ values in Fig. 12g are only slightly greater than 6.0 m $s^{-1}$. Most of the extrema in Fig. 18 are found in regions where the vertical velocities in the evolving flow are stronger than those in the steady-forcing simulations. One exception occurs at 5.5 days, 105 km downstream from the crest, where the extremum in $w_\Delta$ centered at $z = 7$ km is produced by the line of strong downdrafts in the steady-forcing solution visible in Fig. 16b. Just as with the 500-m-high mountain, there are significant quantitative differences in the vertical velocities forced by the 2-km-high mountain in the evolving-flow and steady-forcing simulations.

## b. Low-level blocking and downslope winds

Horizontal wind vectors and the potential temperature at $z = 200$ m are plotted in Fig. 19. The retardation of the front by the topography is clearly evident in the low-level temperature field.[8] Prior to the arrival of the cold front, the north–south gradients in the large-scale flow are relatively weak at 4.5 days (Fig. 4a), and $\tilde{N}h_0/\tilde{U}$ takes similar values of 2.1 and 2.3 in the northern and southern cross sections, respectively (Table 1). In response, the flow is blocked along the entire windward slope; downslope winds of roughly 24 m $s^{-1}$ are present along the full north–south extent of the lee slope, and a distinct pool of warm subsided air is evident downstream of the ridge. Owing to the influence of the Coriolis force, upstream flow splitting occurs very close to the southern

---

[8] Note the change in the color scale for $\theta$ between Figs. 19a and panels Figs. 19b–d.

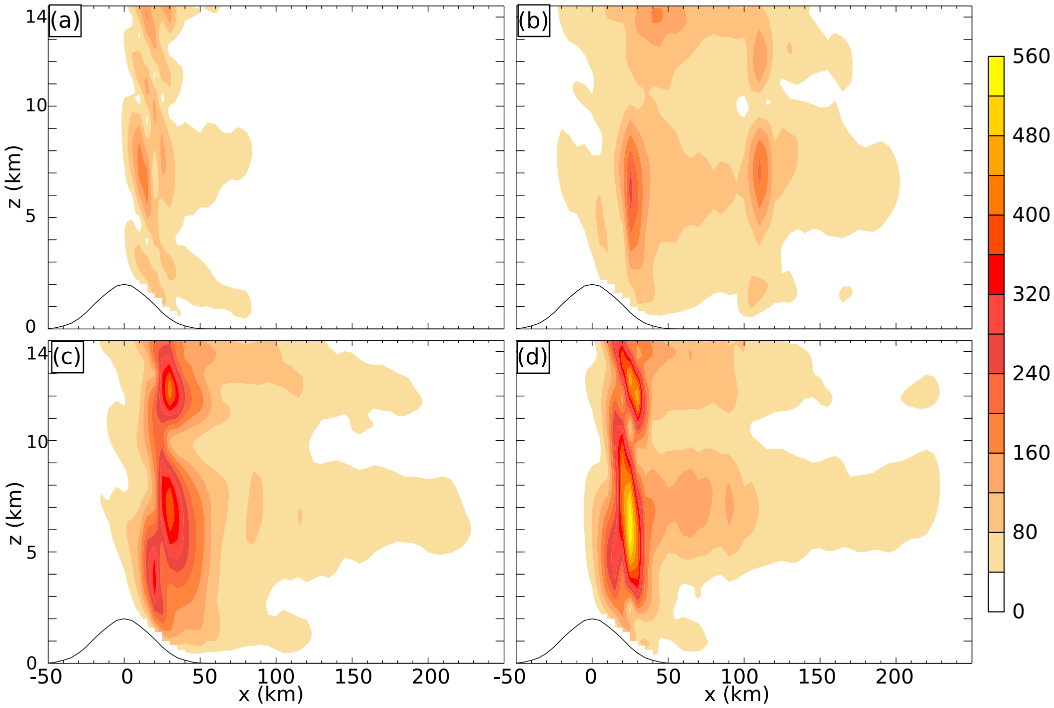

FIG. 18. As in Fig. 10, but for differences between the evolving-flow and steady-forcing simulations for the 2-km-high mountain. The contour interval is now 40 cm $s^{-1}$.

end of the ridge, as might be expected when $\tilde{N}h_0/\tilde{U} \approx 2$ and a horizontally uniform flow impinges on the mountain at a right angle to the ridge axis (Ólafsson and Bougeault 1997; Zängl 2004).

At 5.5 days, as the cold front is just passing beyond the southern end of the ridge, the winds aloft are much stronger, and the north–south position of the jet axis is almost centered over the mountain. Below 4 km, the winds are stronger and the static stability weaker over the northern part of the ridge (Fig. 4b), and, as a consequence, the values of $\tilde{N}h_0/\tilde{U}$ for the northern and southern cross sections are 1.3 and 1.8, respectively. Very different low-level circulations develop adjacent to the northern and southern halves of the ridge (Fig. 19b). The tendency for postfrontal low-level winds to blow from the northwest helps oppose the northern branch of the blocked flow upstream, and the flow now splits around $y = -500$ km, close to the centerline of the mountain. The northern branch of the upstream flow crosses the mountain with only minimal lateral diversion, generating 28 m $s^{-1}$ winds in the lee. The southern branch is diverted around the southern edge of the ridge. This flow is bordered on the north by a convergence line formed by an anticyclonic eddy in the lee of the mountain, in contrast to the classic lee-vortex problem, where the circulation in this eddy would be expected to be cyclonic (Smolarkiewicz and Rotunno 1989).

Significant north–south variations remain in the low-level flow at 6.5 days, when the postfrontal values of $\tilde{N}h_0/\tilde{U}$ for the northern and southern cross sections have increased to 1.6 and 1.9, respectively. The flow encountering the upstream slope splits near $y = -600$ km (Fig. 19c). The cross-ridge flow remains more vigorous in the north, with 36 m $s^{-1}$ winds occurring near the bottom of the lee slope. The southern branch is blocked, with strong winds blowing around the southern tip of the ridge and a region of largely stagnant air in the lee. By 7.5 days, $\tilde{N}h_0/\tilde{U}$ is again more uniform along the ridge, with values of 2.4 and 2.5 in the northern and southern cross sections, respectively (Fig. 19d). The response is again roughly uniform along the ridge, with lee slope winds of 20 m $s^{-1}$ and upstream flow separation near the southern end of the ridge.

Although they are not found at the 200-m level plotted in Figs. 19b and 19c, at higher elevations on the lee slope (such as $z = 750$ m), strong downslope winds are present along the entire north–south extent of the ridge at 5.5 and 6.5 days. As is evident in a comparison of the isentrope spacing just above the lee slope in Figs. 12c and 12e with Figs. 12d and 12f, before reaching the bottom of the lee slope, the shooting flow in the southern cross section terminates abruptly in a jumplike feature with strong upward velocities. In contrast, the high-wind region in the northern cross section extends out over the flatlands.

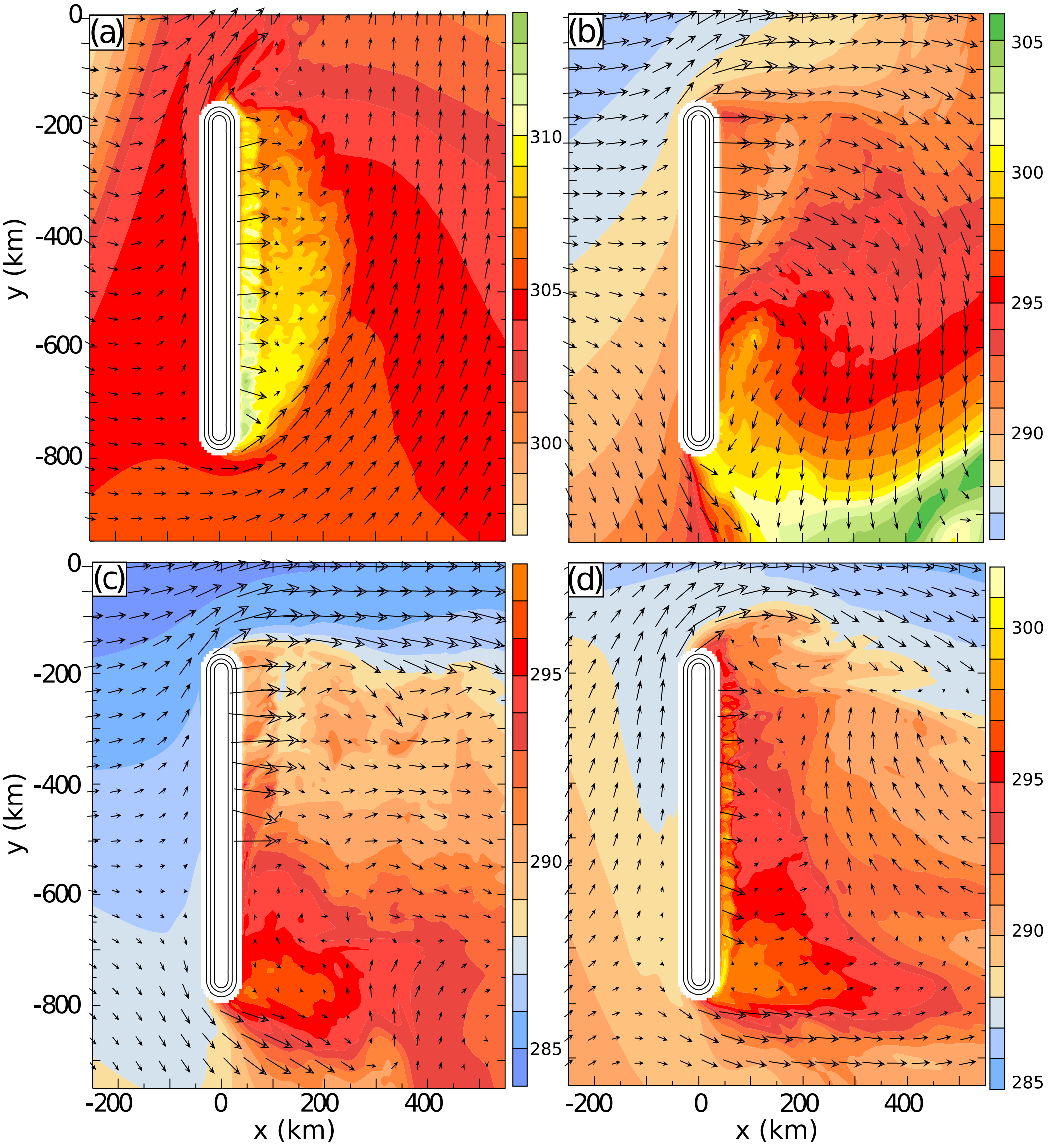

FIG. 19. Contours of $\theta$ (colors; 1-K intervals) and horizontal wind vectors at $z = 200$ m and times (a) 4.5, (b) 5.5, (c) 6.5, and (d) 7.5 days from the 2-km-mountain simulation. Note the change in the color scale for $\theta$ between (a) and (b)–(d). The terrain is contoured at 0.5, 1, and 1.5 km.

This difference in the behavior of the downslope winds near the bottom of the lee slope is illustrated in Fig. 20, which shows the temperature and wind speed at a pair of points 200 km north and south of the center of the mountain, 50 km downstream of the crest (at an approximate elevation of 200 m). A strong mountain wave develops between 3.75 and 4 days, and air parcels traversing this wave undergo roughly 1.5 km of net subsidence, producing strong warming in both the north and the south as they descend near the surface (not shown). Shortly after the temperatures start to rise, downslope winds penetrate down to $z = 200$ m. In the south, the downslope winds cease by 5.5 days as the temperatures once again cool. In the north, on the other hand, the winds remain strong for the remainder of the period, except for a couple hours during the frontal passage around 5 days 3 h (the time shown in Fig. 21c). After the frontal passage in the north, cold downslope winds blow down the lee slope and out into the plains, where the temperature is roughly 5°C colder than in the south. As in the downslope winds earlier in the simulation, the air parcels descending the lee slope in the north experience net subsidence (about 1 km) as they cross the ridge, but the winds are now much colder because, after the frontal passage, the potential temperature in the upstream layer from which these winds originate drops by roughly 15°C. Just after 6 days, several bursts of particularly strong winds occur in the north, in phase with spikes in the temperature that appear to be associated with short periods of enhanced subsidence in the cross-mountain flow.

At the surface, the progressive north-to-south movement of the cold front in the lee is temporarily delayed by the persistence of warm downslope winds along the lee slope, particularly along the northern half of the barrier. This is evident in Fig. 21a, which shows the potential temperature and horizontal wind vectors at the surface around the northern half of the mountain 4 days 21 h into the simulation. Roughly 40 km downstream from the foot of the lee slope, the cold front has penetrated to $y = -300$ km, while warm downslope winds occur in the swath of air closer to the ridge. Along a north–south-oriented convergence line at the terminus of these downslope winds, the vertical velocities at $z = 1.5$-km range between 1 and 2.5 m s$^{-1}$ (Fig. 21d). Three hours later, the downslope winds continue in the same region, but they now occur in cold air that has crossed the mountain; the warmest air lies along a narrow north–south strip downstream of the high-wind region, and the vertical velocities above the convergence line have strengthened (Figs. 21b,e). By 5 days 3 h, the leeward extent of the downslope winds is greatly reduced, and surface cold air has entered the region from both the west and the east (Fig. 21c). The line of strong upward motion has also retreated and now lies above the lower lee slopes but remains very intense near $y = -350$ km (Fig. 21f).

During this period, the extent and strength of the downslope winds and the velocities in the low-level updrafts are all strongly modulated by fluctuations in the structure of the mountain wave over the northern half of the ridge. This is illustrated in Fig. 22 by vertical cross sections of $u$, $w$, and $\theta$ along $y = -380$ km (the location of the northern east–west cross sections shown in Fig. 12). At 4 days 21 h, high surface winds extend almost 100 km downstream of the crest, with wave breaking and patches of reversed flow just above the high-wind layer. Three hours later, the high winds are stronger, but extend only 50 km downstream from the crest, and the extent of the reversed flow in the low-level wave breaking region is much smaller. Strong low-level easterlies are present downstream of $x = 50$ km; these easterlies help the cold front that has wrapped around the north end of the mountain move in from the east. Some combination of the nonlinear mountain wave dynamics and the low-level easterly flow leads to a significant retreat of the downslope wind up the lee slope by 5 days 3 h. Although the high-wind region is much more localized (Fig. 22e), the mountain wave has also become much more intense, with maximum surface winds of greater than 50 m s$^{-1}$ and updraft velocities exceeding 10 m s$^{-1}$ (Fig. 22f). Low-level wave breaking has ceased, but there is an elevated region of reversed flow between the heights of 6 and 8 km.

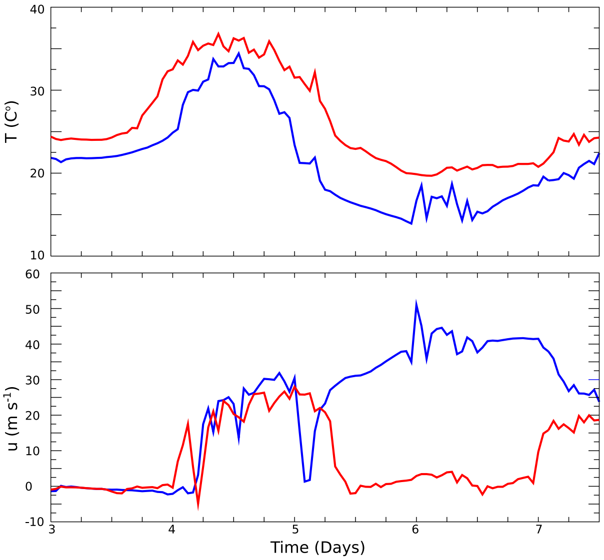

FIG. 20. (a) Temperatures and (b) surface wind speeds as a function of time for two points 50 km downstream of the crest of the 2-km-high mountain where the local terrain elevation is approximately 200 m. Blue (red) curves show data for the point 200 km north (south) of the center of the mountain.

Features such as strong downslope winds in the warm air during the leeside frontal passage and the movement of cold air into the lee from the east have been observed during cold-frontal passages in the lee of the northern Colorado Front Range (Young and Johnson 1984; Neiman et al. 2001). Nevertheless, the Colorado events are clearly influenced by additional topographic features not present in our simulation, including mesoscale terrain features (the Cheyenne Ridge and the Palmer Lake Divide) and the much greater horizontal extent of the Rocky Mountains, which prevents cold air from actually crossing over the ridge as easily as it ultimately does in our simulation.

## 6. Conclusions

This paper depicts the evolution of mountain waves generated by an evolving midlatitude cyclone, an environment more complex than that considered in previous studies of idealized mountain waves, downslope winds, and upstream blocking. The simulations of the evolving large-scale flow over a 500-m-high ridge

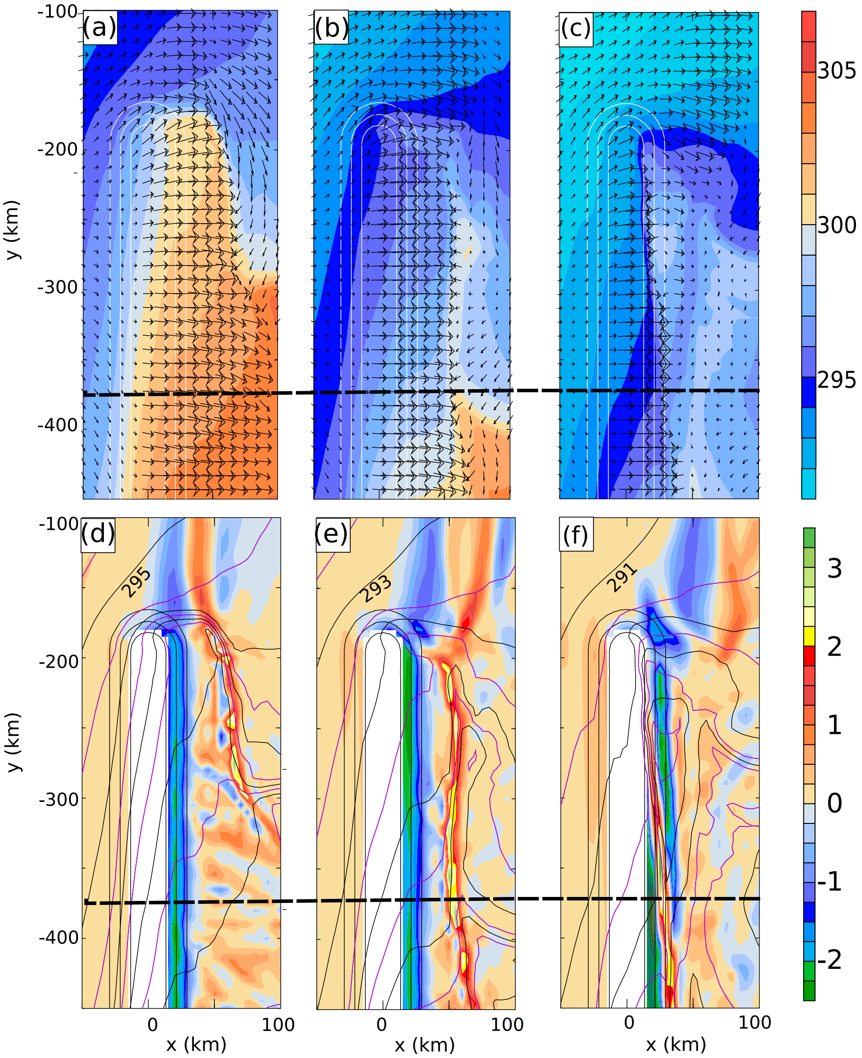

FIG. 21. Penetration of the cold air into the lee in the north. (a)–(c) Surface potential temperature $\theta$ (colors at 1-K intervals) and surface wind vectors. (d)–(f) Vertical velocities at $z = 1.5$ km (colors at 0.25 m s$^{-1}$ intervals) and surface potential temperature $\theta$ (alternating black and violet lines at 1-K intervals). Data are plotted at (a),(d) 4 days 21 h; (b),(e) 5 days; and (c),(f) 5 days 3 h. The terrain is contoured at 0.5, 1, and 1.5 km. The thick dashed line shows the location of the vertical cross section in Fig. 22.

show a progression from weak waves that are relatively uniform along the length of the ridge early on to more complex patterns with significant north–south contrasts between the waves in east–west cross sections 200 km apart during a 2-day period after the cold front has crossed the mountain. Much of this north–south variation follows the north–south shift of the jet maximum above the ridge. A series of steady-state simulations of the cross-ridge flow, both 2D and 3D, forced by the large-scale conditions 200-km upstream of the crest did not faithfully reproduce the wave structures generated by the evolving large-scale flow. Prior to (at 4.5 days) and long after frontal passage (at 7.5 days), when there was minimal north–south variation in the waves along the topography, the amplitude of the waves forced by the evolving upstream flow did not show a consistent relation to the waves forced by steady upstream flows. At 4.5 days, the steady-forcing simulations produced stronger waves than those generated by the evolving large-scale flow, whereas at 7.5 days, the waves generated by the evolving large-scale flow were stronger. At intermediate times of 5.5 and 6.5 days (both after the front had passed the mountain), the amplitudes in the northern and southern cross sections in the steady-upstream-forcing cases again did not systematically reflect the amplitudes and

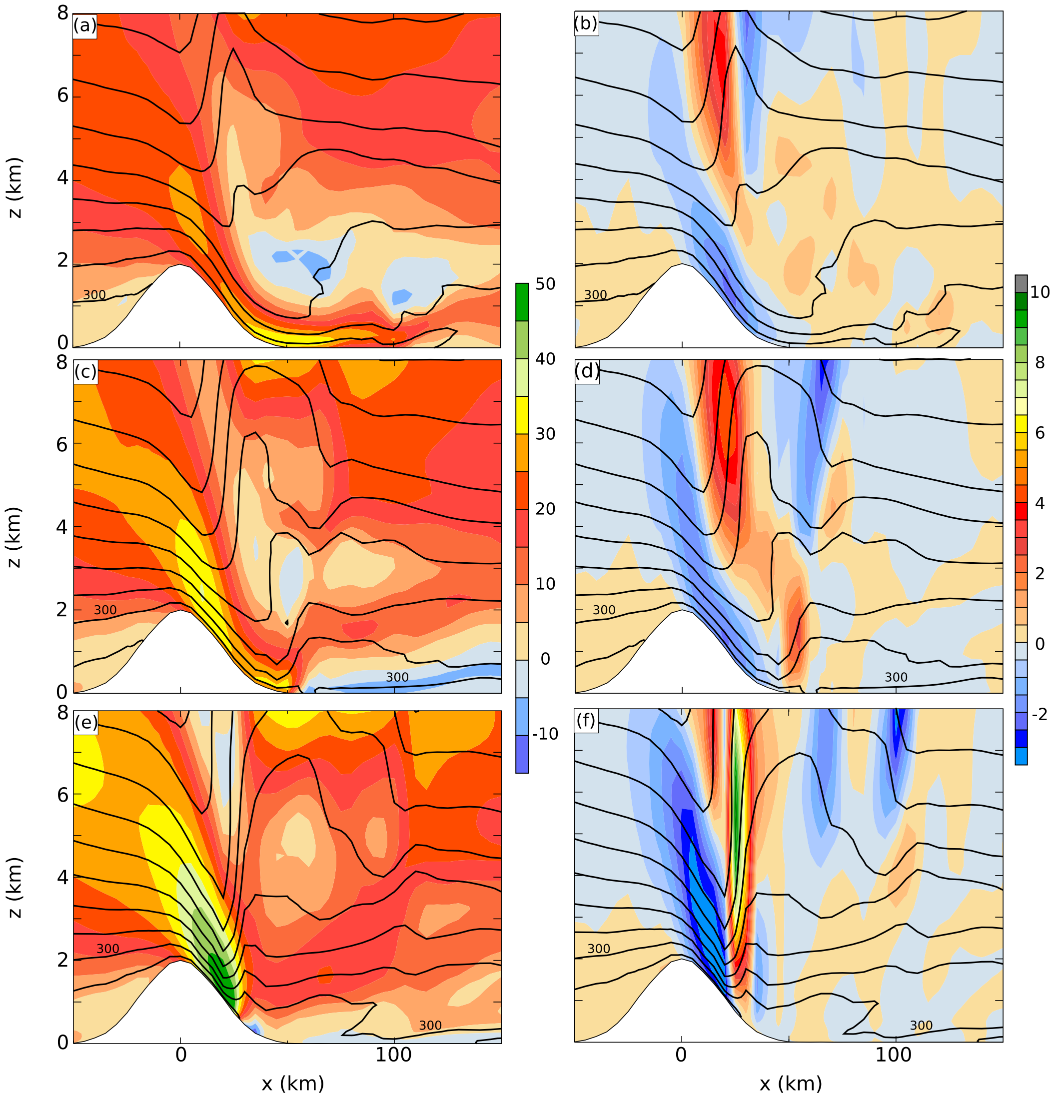

FIG. 22. Vertical cross sections along the dashed line shown in Fig. 21 at times (a),(b) 4 days 21 h; (c),(d) 5 days; and (e),(f) 5 days 3 h. Isentropes at 4-K intervals plotted with (left) contours of $u$ (colors at 5 m s$^{-1}$ intervals) and (right) contours of $w$ (colors at 0.5 m s$^{-1}$ intervals).

flow morphologies in the evolving-forcing simulation. Compare, for example, the 3D simulations with evolving or steady forcing in the south at 5.5 days (Figs. 7a,c) or in the north at 6.5 days (Figs. 8b,d). The along-ridge-averaged RMSD $w_\Delta$ between the evolving flow and associated 3D simulations with steady upstream forcing is large compared to vertical velocities themselves, particularly at 6.5 days.

In simulations with a 2-km-high mountain, the differences between the waves in the northern and southern cross sections, 200 km apart, can be pronounced. While some of this difference is linked to the gradual north–south shifts in the jet above the topography, a persistent difference develops in the low-level updrafts at the terminus of the region of strong downslope winds. The leeward extent of the downslope winds is much shorter in the south, and they end at a jumplike feature with a much stronger low-level updraft than that found in the north. One unique aspect of the waves forced by the 2-km-high mountain is that the horizontal distribution of the vertical velocity field in the upper troposphere shows several linear features angling downstream of the topography in a pattern roughly reminiscent of features observed downstream of the Colorado Front Range. These linear features were not reproduced in steady 3D simulations with north–south (and vertical) shear in the large-scale flow matching the conditions in the evolving flow just upstream of the mountain.

Early and late in the simulation, when the north–south gradients in the large-scale flow encountering the topography are smallest, most of the low-level blocked flow is diverted around the northern end of the ridge in a manner similar to that identified in previous studies of horizontally uniform flows interacting with long ridges when Coriolis forces are nontrivial (Ólafsson and Bougeault 1997; Zängl 2004). In contrast, the blocked flow splits much closer to the north–south center of the ridge at 5.5 and 6.5 days, when the local values of the nonlinearity parameter $\tilde{N}h_0/\tilde{U}$ are lower in the north than in the south. In the immediate lee of the ridge, the penetration of the cold front southward around the northern end of the ridge is delayed by the presence of warm downslope winds. The warm air at the base of the lee slope is eventually pinched off by cold air that traverses the ridge from the west and a second push of cold air that arrives from the east.

One of our main objectives in conducting these simulations is to examine the influence of these terrain-induced disturbances on the cyclone, the jet, and the upper-level wave pattern. A follow-on paper is in preparation that examines the cross-mountain pressure drag, the vertical momentum flux profiles, the momentum budget in regions of wave breaking, and the resulting modifications to the large-scale evolving flow.

*Acknowledgments.* The paper was improved by helpful comments from three anonymous reviewers. This research was supported by Grants AGS-1138977 and AGS-1545927 from the National Science Foundation. Author Menchaca was also supported by a National Science Foundation Graduate Research Fellowship. We would like to acknowledge high-performance computing support from Yellowstone (ark:/85065/d7wd3xhc) provided by NCAR's Computational and Information Systems Laboratory, sponsored by the National Science Foundation.

## REFERENCES

Bacmeister, J. T., and M. Schoberl, 1989: Breakdown of vertically propagating two-dimensional gravity waves forced by orography. *J. Atmos. Sci.*, **46**, 2109–2134, doi:10.1175/1520-0469(1989)046<2109:BOVPTD>2.0.CO;2.

——, P. A. Newman, B. L. Gary, and K. R. Chan, 1994: An algorithm for forecasting mountain wave–related turbulence in the stratosphere. *Wea. Forecasting*, **9**, 241–253, doi:10.1175/1520-0434(1994)009<0241:AAFFMW>2.0.CO;2.

Brinkmann, W. A. R., 1971: What is a foehn? *Weather*, **26**, 230–240, doi:10.1002/j.1477-8696.1971.tb04200.x.

Chen, C.-C., D. R. Durran, and G. Hakim, 2005: Mountain-wave momentum flux in an evolving synoptic-scale flow. *J. Atmos. Sci.*, **62**, 3213–3231, doi:10.1175/JAS3543.1.

——, G. J. Hakim, and D. R. Durran, 2007: Transient mountain waves and their interaction with large scales. *J. Atmos. Sci.*, **64**, 2378–2400, doi:10.1175/JAS3972.1.

Doyle, J., Q. Jiang, R. Smith, and V. Grubišić, 2011: Three-dimensional characteristics of stratospheric mountain waves during T-REX. *Mon. Wea. Rev.*, **139**, 3–23, doi:10.1175/2010MWR3466.1.

Durran, D. R., and J. B. Klemp, 1983: A compressible model for the simulation of moist mountain waves. *Mon. Wea. Rev.*, **111**, 2341–2361, doi:10.1175/1520-0493(1983)111<2341:ACMFTS>2.0.CO;2.

Hakim, G., 2000: Role of nonmodal growth and nonlinearity in cyclogenesis initial-value problems. *J. Atmos. Sci.*, **57**, 2951–2967, doi:10.1175/1520-0469(2000)057<2951:RONGAN>2.0.CO;2.

Hills, M. G., and D. R. Durran, 2012: Nonstationary trapped lee waves generated by the passage of an isolated jet. *J. Atmos. Sci.*, **69**, 3040–3059, doi:10.1175/JAS-D-12-047.1.

Hong, S.-Y., Y. Noh, and J. Dudhia, 2006: A new vertical diffusion package with an explicit treatment of entrainment processes. *Mon. Wea. Rev.*, **134**, 2318–2341, doi:10.1175/MWR3199.1.

Hughes, M., A. Hall, and R. G. Fovell, 2009: Blocking in areas of complex topography, and its influence on rainfall distributions. *J. Atmos. Sci.*, **66**, 508–518, doi:10.1175/2008JAS2689.1.

Kim, Y.-J., S. D. Eckermann, and H.-Y. Chun, 2003: An overview of the past, present and future of gravity-wave drag parametrization for numerical climate and weather prediction models. *Atmos.-Ocean*, **41**, 65–98, doi:10.3137/ao.410105.

Klemp, J., J. Dudhia, and A. Hassiotis, 2008: An upper gravity-wave absorbing layer for NWP applications. *Mon. Wea. Rev.*, **136**, 3987–4004, doi:10.1175/2008MWR2596.1.

Lilly, D. K., and J. B. Klemp, 1979: The effects of terrain shape on nonlinear hydrostatic mountain waves. *J. Fluid Mech.*, **95**, 241–261, doi:10.1017/S0022112079001452.

Lott, F., and H. Teitelbaum, 1993a: Linear unsteady mountain waves. *Tellus*, **45A**, 201–220, doi:10.1034/j.1600-0870.1993.t01-2-00004.x.

——, and ——, 1993b: Topographic waves generated by a transient wind. *J. Atmos. Sci.*, **50**, 2607–2624, doi:10.1175/1520-0469(1993)050<2607:TWGBAT>2.0.CO;2.

Lynch, P., 1997: The Dolph–Chebyshev window: A simple optimal filter. *Mon. Wea. Rev.*, **125**, 655–660, doi:10.1175/1520-0493(1997)125<0655:TDCWAS>2.0.CO;2.

Neiman, P. J., F. Martin Ralph, R. L. Weber, T. Uttal, L. B. Nance, and D. H. Levinson, 2001: Observations of nonclassical frontal propagation and frontally forced gravity waves adjacent to steep topography. *Mon. Wea. Rev.*, **129**, 2633–2659, doi:10.1175/1520-0493(2001)129<2633:OONFPA>2.0.CO;2.

Ólafsson, H., and P. Bougeault, 1997: The effect of rotation and surface friction on orographic drag. *J. Atmos. Sci.*, **54**, 193–210, doi:10.1175/1520-0469(1997)054<0193:TEORAS>2.0.CO;2.

Reinecke, P., and D. Durran, 2008: Estimating topographic blocking using a Froude number when the static stability is nonuniform. *J. Atmos. Sci.*, **65**, 1035–1048, doi:10.1175/2007JAS2100.1.

Rotunno, R., W. Skamarock, and C. Snyder, 1994: An analysis of frontogenesis in numerical simulations of baroclinic waves. *J. Atmos. Sci.*, **51**, 3373–3398, doi:10.1175/1520-0469(1994)051<3373:AAOFIN>2.0.CO;2.

Schemm, S., H. Wernli, and L. Papritz, 2013: Warm conveyor belts in idealized moist baroclinic wave simulations. *J. Atmos. Sci.*, **70**, 627–652, doi:10.1175/JAS-D-12-0147.1.

Skamarock, W., and Coauthors, 2008: A description of the Advanced Research WRF version 3. NCAR Tech. Note NCAR/TN-475+STR, 113 pp., doi:10.5065/D68S4MVH.

Smith, R., B. Woods, J. Jensen, W. Cooper, J. Doyle, Q. Jiang, and V. Grubišić, 2008: Mountain waves entering the stratosphere. *J. Atmos. Sci.*, **65**, 2543–2562, doi:10.1175/2007JAS2598.1.

Smolarkiewicz, P. K., and R. Rotunno, 1989: Low Froude number flow past three dimensional obstacles. *J. Atmos. Sci.*, **46**, 1154–1164, doi:10.1175/1520-0469(1989)046<1154:LFNFPT>2.0.CO;2.

Waite, M., and C. Snyder, 2009: The mesoscale kinetic energy spectrum of a baroclinic life cycle. *J. Atmos. Sci.*, **66**, 883–901, doi:10.1175/2008JAS2829.1.

Wells, H., S. Webster, and A. Brown, 2005: The effect of rotation on the pressure drag force produced by flow around long mountain ridges. *Quart. J. Roy. Meteor. Soc.*, **131**, 1321–1338, doi:10.1256/qj.04.37.

Young, G. S., and R. H. Johnson, 1984: Meso- and microscale features of a Colorado cold front. *J. Climate Appl. Meteor.*, **23**, 1315–1325, doi:10.1175/1520-0450(1984)023<1315:MAMFOA>2.0.CO;2.

Zängl, G., 2004: Upstream effects of an Alpine-scale mountain range under various flow angles. *Meteor. Z.*, **13**, 291–296, doi:10.1127/0941-2948/2004/0013-0291.